

# Collimator effects in proton planning

**Evangelos Matsinos**

Varian Medical Systems Imaging Laboratory GmbH, Täfernstrasse 7, CH-5405  
Baden-Dättwil, Switzerland

E-mail: [evangelos.matsinos@varian.com](mailto:evangelos.matsinos@varian.com) ‡

**Abstract.** The present paper pertains to corrections which are due to the presence of beam-limiting and beam-shaping devices in proton planning. Two types of corrections are considered: those originating from the nonzero thickness of such devices (geometrical effects) and those relating to the scattering of beam particles off their material. The application of these two types of corrections is greatly facilitated by decomposing their effects on the fluence into easily-calculable contributions. To expedite the derivation of the scattering corrections, a two-step process has been introduced into a commercial product which is widely used in planning (Treatment Planning System Eclipse<sup>(TM)</sup>). The first step occurs at the beam-configuration phase and comprises the analysis of half-block fluence measurements and the extraction of the one parameter of the model which is used in the description of the beamline characteristics; subsequently, a number of Monte-Carlo runs yield the parameters of a convenient parameterisation of the relevant fluence contributions. The second step involves (at planning time) the reconstruction of the parameters (which are used in the description of the scattering contributions) via simple interpolations, performed on the results obtained during the beam-configuration phase. Given the lack of dedicated data, the validation of the method is currently based on the reproduction of the parts of the half-block fluence measurements (i.e., of the data used as input during the beam configuration) which had been removed from the database to suppress unwanted (block-scattering) contributions; it is convincingly demonstrated that the inclusion of the scattering effects leads to substantial improvement in the reproduction of the experimental data. The contributions from the block-thickness and block-scattering effects (to the fluence) are presented separately in the case of a simple water phantom; in this example, the maximal contribution of the two block-relating effects amounts to a few percent of the prescribed dose.

PACS numbers: 87.55.Gh, 87.55.kh, 87.56.jk, 87.56.nk

*Keywords:* particle therapy, proton, block, collimator, slit, corrections, scattering

## 1. Introduction

To shape the beam so that it matches the characteristics of the specific treatment in radiation therapy (thus achieving the delivery of the prescribed dose to the target

‡ E-mail address after December 31, 2008: [evangelos\[dot\]matsinos\[at\]sunrise\[dot\]ch](mailto:evangelos[matsinos@sunrise]ch)

(tumour) and maximal protection of the surrounding healthy tissue and vital organs), beam-limiting and beam-shaping devices (BL/BSDs) are routinely used. Generally speaking, the beam is first restricted (in size) by the primary collimator, a beam-limiting device giving it a rectangular shape. The beam may subsequently encounter the multi-leaf collimator (MLC), which may be static or dynamic (i.e., undergoing software-controlled motion during the treatment session). More frequently than not, the desirable beam shaping is achieved by inserting a metallic piece (with the appropriate aperture and thickness) into the beamline, directly in front of the patient; this last beam-shaping device is called a patient collimator or simply a block. Being positioned close to the patient, the block achieves efficient fall-off of the dose (sharp penumbra) outside the target area. (The simultaneous use of MLC and block is not common.)

To provide efficient attenuation of the beam outside the irradiated volume, the BL/BSDs are made of high- $Z$  materials. The primary collimator and the MLC are fixed parts of the treatment machine, whereas the block not only depends on the particular patient, but also on the direction from which the target is irradiated. Therefore, there may be several blocks in one treatment plan, not necessarily corresponding to the same thickness or (perhaps) material.

The presence of BL/BSDs in treatment plans induces three types of physical effects:

- a) Confinement of the beam to the area corresponding to full transmission (i.e., to the aperture of the device).
- b) Effects associated with the nonzero thickness of the device (geometrical effects).
- c) Effects relating to the scattering of the beam off the material of the device.

Type-(a) effects (direct blocking of the beam) are dominant and have always been taken into account. The standard way to do this is by reducing the BL/BSD into a two-dimensional (2D) object (i.e., by disregarding its thickness) and assuming no transmission of the beam outside its aperture. Type-(b) and type-(c) effects induce corrections which, albeit at a few-percent level of the prescribed dose, may represent a sizable fraction of the *local* dose; due to their complexity and to time restrictions during the planning phase, these corrections have (so far) been omitted in clinical applications.

The subject of the slit scattering in beam collimation was first addressed by Courant (1951). Courant extracted analytical solutions for the effective increase in the slit width (attributable to scattering) by solving the diffusion equation inside the collimator. To fulfill the boundary conditions, he introduced the negative-image technique, which was later criticised (e.g., by Burge and Smith (1962)). Despite the debatable usefulness of the practical use of Courant's work, that article set forth definitions which were employed in future research; for example, by categorising the scattered particles as:

- those impinging upon the upstream face of the collimator and emerging from its inner surface (bore),
- those entering the bore and scattering out of it, and
- those entering the bore and leaving the downstream face of the collimator.

In the present paper, Courant's type-1 particles will correspond to our 'outer tracks' (OTs), type-2 particles to our 'bore-scattered inner tracks' (BSITs), and type-3 particles to our 'going-through inner tracks' (GTITs), see Fig. 1. The tracks which do not hit the block will comprise the 'pristine' beam.

Aiming at the determination of the optimal material for proton-beam collimation and intending to provide data for experiments at the linear accelerator of the National Institute for Research in Nuclear Science (NIRNS) at Harwell, Burge and Smith (1962) re-addressed the slit-scattering problem and obtained a solution via the numerical integration of the diffusion equation. Burge and Smith reported considerable differences to Courant's results. In the last section of their article, the authors discussed alternative approaches to the slit-scattering problem.

A Monte-Carlo (MC) method, as a means to study the collimator-scattering effects, was introduced by Paganetti (1998). Using the GEANT code to simulate a proton beamline at the Hahn-Meitner Institut (HMI) in Berlin, Paganetti introduced simple parameterisations to account for the changes in the energy and angular divergence of the beam as it traverses the various beamline elements. Judging from Fig. 6 of that paper, one expects the scattering effects to be around the 1% level. In the last section of his article, Paganetti correctly predicted that 'Monte-Carlo methods will become important for providing proton phase-space distributions for input to treatment-planning routines, though the calculation of the target dose will still be done analytically.' Our strategy is similar to that of Paganetti: the dose, delivered by the pristine beam, will be corrected for scattering effects on the basis of results obtained via MC runs prior to planning (actually, when the particular proton-treatment machine is configured).

Block scattering was also investigated, along the general lines of Paganetti's paper, in the work of van Luijk *et al* (2001). The (same version of the) GEANT code was used, to simulate a proton beamline at Kernfysisch Versneller Instituut (KVI) in Groningen, and the characteristics of the scattered protons were studied. To validate their approach, the authors obtained dose measurements for several field sizes and at several distances from the block. Unlike other works, the effect of scattering in air was also included in that study, and turned out to be more significant than previously thought (its contribution to the angular divergence of the beam exceeded 1 mrad per 1 m of air). One of the interesting conclusions of that paper was that the penumbra of the dose distribution is mostly accounted for by the lateral spread of the undisturbed beam; that conclusion somewhat allayed former fears that the extraction of the effective-source size ( $\sigma_s$ ) and of the effective source-axis distance (SAD), both obtained from measurements conducted in the presence of a block, might be seriously affected by block-scattering contributions. Finally, the paper addressed the asymmetries induced by a misalignment of the block, concluding that they might be sizable.

In their recent work, Kimstrand *et al* (2008) put the emphasis on the scattering off the multi-leaf collimator (MLC). In their approach, they also obtain the values of the parameters (involved in their corrections) by using a MC GEANT-based method. In their Section 'Discussion and Conclusions', the authors, setting forth the future

perspectives, mention that ‘a challenge . . . is to implement collimator scatter for a pencil beam kernel dose calculation engine.’ We agree on this being ‘a challenge’. The authors then advance to pre-empt that ‘. . . the methods presented . . . can straightforwardly be applied to arbitrary shaped collimators of different materials, such as moulded patient-specific collimators used in passively scattered proton beams.’ One should at least remark that their paper does not contain adequate information supporting the thesis that the proposed approach is of practical use in a domain where the execution time is a important factor.

## 2. Method

In the present paper, the standard ICRU (1987) coordinate system will be used; in beam’s eye view, the  $x$  axis points to the right,  $y$  upward, and  $z$  toward the source. The origin of the coordinate system is the isocentre.

### 2.1. Miniblocks

Assuming vanishing transmission outside the aperture of the BL/BSD, all relevant contributions to the fluence involve 2D integrals over its area. The evaluation of such integrals is time-consuming; at a time when serious efforts are made to reduce the overall time allotted to each patient, the generous allocation of resources in the evaluation and application of *corrections* to the primary dose is unacceptable. To expedite the extraction of these corrections, one must find a fast way to decompose the effects of a 2D object (e.g., of the aperture of the BL/BSD) into one-dimensional, easily-calculable, easily-applicable contributions.

An example of one such 2D object is shown in Fig. 2; the area B represents the aperture (corresponding to full transmission of the beam) and is separated from the area A, representing the (high- $Z$ ) material, via the contour C. Full attenuation of the beam is assumed in the area A. The contour C and the ‘outer’ contour of the area A (which is not shown) may have any arbitrary shape (e.g., rectangular, circular, etc.); the only requirement is that the contour C be contained within the contour of the area A.

Let us assume that the aim is to derive the influence of the BL/BSD at one point Q (Fig. 3); the point Q is projected to the point P, on the BL/BSD plane. The point P may be contained in the interior or the exterior of the area B.

*2.1.1. The point P lies within the area B* To enable the evaluation of the effects of the BL/BSD at the point Q, a set of  $N$  directions on the BL/BSD plane, intersecting at the point P, are chosen; an example with  $N = 4$  is shown in Fig. 4. The effects of the BL/BSD at the point Q will be evaluated from the elementary contributions of the line segments corresponding to the intersection of  $N$  straight lines with the contour C. These line segments, which are contained within the area B and are bound by the contour C, will be called *miniblocks*. The effect of the BL/BSD at the point Q will be evaluated by

averaging the elementary contributions of the miniblocks created around the point P. In Fig. 4, one of these miniblocks is represented by the line segment  $S_1S_2$ . Obviously, the number of miniblocks in each direction depends on the number of intersections of the straight line (drawn through the point P, parallel to the chosen direction) and the contour C.

*2.1.2. The point P lies outside the area B* As in the previous section, a set of  $N$  directions, intersecting at the point P, are chosen; an example with  $N = 4$  is shown in Fig. 5. Again, the effects of the BL/BSD at the point Q will be evaluated on the basis of the elementary contributions in these  $N$  directions. In Fig. 5, one of the miniblocks is denoted by  $S_3S_4$ .

*2.1.3. General remarks* Evidently, the number of directions  $N$  is arbitrary. For fixed  $N$ , the accuracy of the evaluation depends on the details of the contour C and on the proximity of the point P to it. The reliability of the estimation is expected to increase with  $N$ . (The evaluation is exact for  $N \rightarrow \infty$ .)

There is one difference between the cases described in Sections 2.1.1 and 2.1.2. In case that the point P lies within the area B, there will always be at least one miniblock per direction; if the point P lies outside the area B, there might be no intersections with the contour C in some directions (in which case, the corresponding elementary contributions vanish).

Let us assume that the physical characteristics of the beam (lateral spread, angular divergence, energy, etc.) and the entire geometry (also involving the BL/BSD) are fixed. Apart from the original point Q, the elementary contributions will involve (the coordinates of) three additional points: the two end points of the particular miniblock and the point P. Due to the fact that the  $N$  directions are created around the point P, the two end points of every miniblock and the point P will always lie on one straight line. If the point P lies within the area B, it may lie within or outside a miniblock. On the other hand, if the point P lies outside the area B, it will always lie outside any corresponding miniblock. In any case, the elementary contribution of a miniblock will generally be a function of the distance of its two end points to the point P. Additionally, the elementary contribution of a miniblock to the point Q will also involve the distance of the point Q to the BL/BSD plane, denoted as  $z$  in Fig. 3.

A few remarks are worth making.

- The angle between consecutive directions may be constant or variable. If the angle is not constant, weights (to the elementary contributions) have to be applied.
- The values of  $N$  in Sections 2.1.1 and 2.1.2 do not have to be the same. Furthermore, different values of  $N$  might be used for the points which are projected onto the interior (or exterior) of the area B, e.g., depending on the proximity of the point P to the contour C.

At present, the method of this paper applies only to BL/BSDs with a constant aperture profile throughout their thickness; to derive the corrections in case of other shapes (e.g., for BL/BSDs with a tapered aperture profile), substantial modifications are required. The approach is applicable to any type of BL/BSD, be it the primary collimator, the MLC, or the block; to derive the corrections, the only input pieces are the physical characteristics of the material (of which the BL/BSD is made) and, naturally, geometrical details. From now on, however, we will restrict ourselves to the effects induced by the block, which (given its proximity to the patient) are expected to be of greater interest and importance in clinical applications. This choice, meant to emphasise importance, should not be seen as a restriction of the method.

## 2.2. Block-thickness corrections

A method for the evaluation of the thickness corrections was recently proposed by Slopsema and Kooy (2006); we will follow their terminology. Thus, ‘downstream (upstream) projection’ will indicate the projection of the downstream (upstream) face of the block on the  $(x,y)$  plane at the specified  $z$  position (depth). Similarly, the ‘extension’ of the block will correspond to the physical block translated in space (from its actual position to the specified depth, parallel to the central beam axis).

In medical applications, the formal beam-shaper object (e.g., the so-called DICOM block), which is created at planning time to represent the physical block, comprises the projection of the *downstream face* (of the block) to a plane (perpendicular to the beam) at isocentre depth. The physical block (extension) is therefore obtained via a simple scaling involving the source-axis and block-isocentre (IBD) distances. Having retrieved the extension of the block, it is straightforward to obtain the downstream projection at any  $z$ ; in order to obtain the upstream projections, one has to use, in addition to the aforementioned quantities, the block thickness ( $d$ ). The relation between the DICOM block, the extension, and the downstream projection at a specified  $z$  position is shown in Fig. 6. The upstream projection is obtained by projecting the extension from depth  $z = \text{IBD} + d$ . The thin-block approximation, which is currently used in clinical applications when evaluating the dose, corresponds to  $d = 0$  mm (the downstream and upstream projections coincide at all  $z$  values).

Assuming that the coordinates of the projected (downstream- or upstream-face, as the case might be) ends of a miniblock are denoted as  $x_1$  and  $x_2$ , the contribution of the miniblock to the fluence at a point  $x_p$  (lying on the straight line defined by  $x_1$  and  $x_2$ ) on the calculation plane is given by the formula

$$F(x_p) = \frac{1}{2} \left| \operatorname{erf}\left(\frac{x_p - x_1}{\sigma_1\sqrt{2}}\right) - \operatorname{erf}\left(\frac{x_p - x_2}{\sigma_2\sqrt{2}}\right) \right|, \quad (1)$$

where  $\operatorname{erf}(x)$  denotes the error function and  $\sigma_{1,2}$  stand for the rms (lateral) spreads of the beam at the specified depth. The quantities  $\sigma_{1,2}$  are obtained via source mirroring according to the method of Slopsema and Kooy (2006); as points on the downstream or upstream faces of the block are used, the resulting  $\sigma$  values in Eq. (1) are equal only

when one block face is involved in the mirroring process.

One simple example of the projections on the calculation plane is shown in Fig. 7; the block extension is contained within the downstream projection, which (in turn) is contained within the upstream projection. In reality, depending on the complexity of the shape of the block aperture and on the relative position of the central beam axis, these three contours might intersect one another. The central beam axis intersects the calculation plane at the origin of the  $(x,y)$  coordinate system. One miniblock is shown (the line segment contained within the block extension), along with two points, one within the miniblock (P), another outside the miniblock (P'). The fluence contributions to both points may be evaluated by using Eq. (1) with the appropriate  $x_{1,2}$  and  $\sigma_{1,2}$  values.

The essentials for the evaluation of the contribution of a miniblock to the fluence at a specified point on the calculation plane are to be found in Fig. 8. Although, in the general case, the miniblock does not contain the intersection of the  $x$  and  $y$  axes of Fig. 7, all lengths (which are important to our purpose) scale by the same factor, thus enabling the simplified picture of Fig. 8.

According to Slopsma and Kooy (2006), the source is mirrored onto the calculation plane by using points either on the downstream or on the upstream face of the block. The values of the mirrored-source size, corresponding to these two options, are given by

$$\sigma_d = \sigma_s \frac{\text{IBD} - z}{\text{SAD} - \text{IBD}} \quad (2)$$

and

$$\sigma_u = \sigma_s \frac{\text{IBD} - z + d}{\text{SAD} - \text{IBD} - d}. \quad (3)$$

The coordinates of the projected points  $U_1$ ,  $D_1$ ,  $D_2$ , and  $U_2$  are obtained on the basis of Fig. 8 via simple operations. The last item needed to derive the contributions to the fluence may be found on page 5444 of the paper of Slopsma and Kooy (2006): ‘Protons whose tracks project inside the aperture extension onto the plane of interest see the upstream face as the limiting boundary. Only for protons whose tracks end up outside the aperture on the plane of interest is the downstream face the limiting aperture boundary.’ In fact, this statement applies to the case of a half-block (one-sided block). The modification, however, in case of a miniblock is straightforward.

- Points within the extension of the aperture see the upstream face of the miniblock as the limiting boundary.
- Points outside the extension of the miniblock see one upstream *and one downstream* edge as limiting boundaries.

Obviously, in order to evaluate the fluence at the point P (Fig. 8), one has to use the coordinates of the projected points  $U_1$  and  $U_2$ , along with  $\sigma_u$  in Eq. (1). On the other hand, to evaluate the fluence at P', one has to use  $U_1$  along with  $\sigma_u$  (contribution of the ‘left’ part of the miniblock) and  $D_2$  along with  $\sigma_d$  (contribution of the ‘right’ part

of the miniblock). This simplified picture, featuring what a point ‘perceives’ as limiting boundaries, suffices in obtaining the appropriate fluence contributions.

Finally, the number of contributions which a point will receive depends on the geometry and on the shape of the block. One example of a point receiving two contributions in a given direction is shown in Fig. 9; the point P lies within the extension of the miniblock on the left and outside the extension of the miniblock on the right. Additionally, one might have to deal with a block with more than one apertures (hence contours). To determine in the present work the appropriate thickness corrections for arbitrary block-aperture shape and beamline geometry, dedicated software was developed.

### 2.3. Block-scattering corrections

Before entering the details of the derivation of the scattering corrections, it is worth providing a concise outline of our approach. First of all, our aim is to obtain a *fast and reliable* solution to the scattering problem; exact analytical solutions are welcome as long as they fulfill this requirement. Second, the solution has to be general enough for direct application to all proton-treatment machines.

To expedite the derivation and application of the corrections at planning time, we will introduce a two-step approach.

- All the parameters which are independent of the specific details of plans will be evaluated during the beam-configuration phase; given a fixed (hardware) setup, every treatment machine is configured only once.
- The corrections for each particular plan will be derived (at planning time) from the existing results (i.e., those obtained at beam-configuration phase) via simple interpolations.

Given that the physics of multiple scattering is known, it is possible to obtain the exact solution for the relevant beam properties (lateral spread, angular divergence) from the beamline characteristics of each treatment machine. However, it is unrealistic to introduce a dedicated process for each supported machine, especially in order to derive corrections to the delivered dose. Additionally, if a dedicated (per-case) approach is implemented in a software product which is intended to support a variety of machine manufacturers, one has to be prepared to allot the necessary resources whenever a new product appears. To avoid these problems and to retain the generality of the approach, one has no other choice but to introduce a simple, adjustable model to account for the beam optics. The model of the present paper has only one parameter, which will be fixed from half-block fluence measurements.

The parameters which achieve the description of the various distributions of the scattered protons are determined via MC runs. These runs take account of the variability in the block material, block thickness, incident energy (energy at nozzle entrance), and nozzle-equivalent thickness (NeT) for all the options (combinations of the hardware components of the beamline, leading to ranges of available energies and of NeTs, as well



as imposing restrictions on the field size) for which a machine is configured. To enable the easy use of the results, the output is put in the form of expansion parameters in two geometrical quantities which are involved in the description of the scattering effects.

The scattering corrections for all the blocks in a plan are determined (at planning time) from the aforementioned results via simple interpolations. The application of the corrections involves the concept of miniblocks, as they have been introduced in Section 2.1 of this paper.

*2.3.1. Modelling of the beam* One model which is frequently used in beam optics features the bivariate Gaussian distribution in the lateral direction  $y$  (distance to the central beam axis) and the (small) angle  $\theta$  (with respect to that axis). (Rotational symmetry is assumed here.)

$$f(y, \theta) = \frac{1}{\pi\sqrt{D}} \exp\left(-\frac{A\theta^2 - 2By\theta + Cy^2}{D}\right), \quad (4)$$

with

$$D = AC - B^2. \quad (5)$$

The parameters  $A$  and  $C$  represent twice the variance in  $y$  and  $\theta$ , respectively. The  $(y, \theta)$  correlation is defined as

$$\rho = \frac{B}{\sqrt{AC}}. \quad (6)$$

The quantity  $\rho$  (which is bound between  $-1$  and  $1$ ) is a measure of the focusing in the beam. Positive  $\rho$  values indicate a defocusing system, negative a focusing one; this becomes obvious after one puts Eq. (4) in the form

$$f(y, \theta) = \frac{1}{\sigma_\theta\sqrt{2\pi}} \exp\left(-\frac{\theta^2}{2\sigma_\theta^2}\right) \frac{1}{\sigma_s\sqrt{2\pi(1-\rho^2)}} \exp\left(-\frac{(y - \rho\frac{\sigma_s}{\sigma_\theta}\theta)^2}{2\sigma_s^2(1-\rho^2)}\right). \quad (7)$$

We now touch on the variation of  $A$ ,  $B$ , and  $C$  along the beam-propagation direction. Assuming that the quantities  $A_0$ ,  $B_0$ , and  $C_0$  denote the corresponding values at isocentre depth and that the beam propagates in air (without scattering),  $A$ ,  $B$ , and  $C$  at distance  $z$  from the isocentre (see Fig. 6) are given by the expressions

$$A(z) = A_0 - 2B_0z + C_0z^2, B(z) = B_0 - C_0z, \text{ and } C(z) = C_0. \quad (8)$$

With these transformations, the joint probability distribution of Eq. (4) is invariant under translations in  $z$ . In case that the beam traverses some material, Eqs. (8) have to be modified accordingly, to take account of the beam broadening due to multiple scattering.

*2.3.2. Simplified parameterisation of the beamline* The accurate modelling of the beam may be obtained on the basis of formulae such as those given in the previous section. In Section 2.3, however, we reasoned that a simplified parameterisation of the beamline is desirable; one additional argument may be put forth.

Currently, as far as proton therapy is concerned, four dose-delivery techniques are in use: single-scattering, double-scattering, uniform-scanning (formerly known as wobbling), and modulated-scanning (formerly simply known as scanning). In the modulated-scanning technique, magnets deflect a narrow beam onto a sequence of pre-established points (spots) on the patient (for pre-determined optimal times), thus ‘scanning’ the (cross section of the) region of interest. Uniform scanning involves the spread-out of the beam using fast magnetic switching. The broadening of the beam in the single-scattering technique is achieved by one scatterer, made of a high- $Z$  material and placed close to the entrance of the nozzle. Currently, the most ‘popular’ technique involves a double-scattering system.

In a double-scattering system, a second scatterer is placed downstream of the first scatterer in order to achieve efficient broadening of the beam; studies of the effects of the second scatterer may be found in the literature, e.g., see Takada (2002) and more recent reports by the same author and Gottschalk. The second scatterer is usually made of two materials: a high- $Z$  (such as lead) material at the centre (i.e., close to the central beam axis), surrounded by a low- $Z$  (such as aluminium, lexan, etc.) material (which is frequently, but not necessarily, shaped as a concentric ring). The arrangement produces more scattering at the centre than the periphery, leading (after sophisticated fine-tuning) to the creation of a broad flat field at isocentre.

To simulate the effect of the second scatterer in the present work,  $(y, \theta)$  events are generated at  $z = \text{SAD}$  as follows. The variable  $y$  is sampled from the Gaussian distribution with mean 0 and variance  $\sigma_s^2$  (the source-size calibration must precede this step);  $\sigma_s$  depends on the incident energy and NeT. To account for the lateral limits of the beam,  $y$  is restricted within the interval  $[-R_L, R_L]$ , where the characteristic length  $R_L$  is taken herein to be the radius of the second scatterer. The variable  $\theta$  is first sampled from the Gaussian distribution with mean 0 and a  $y$ -dependent variance  $\sigma_\theta^2$  according to the formula

$$\sigma_\theta(t) = \sigma_\theta(1) \left( (1 - \lambda) |t| + \lambda \right), \quad (9)$$

where  $t$  denotes the lateral position as a fraction of  $R_L$ ;  $|t| = |y/R_L| \leq 1$ . To account for the  $y$ -dependent bias in  $\theta$ , we then use the transformation  $\theta \rightarrow \theta + \tan^{-1}(y/L) \simeq \theta + y/L$ , where  $L$  stands for the distance between the first scatterer and the source. Obviously,  $\lambda$  denotes the ratio of two  $\sigma_\theta$  values, i.e., the value at the centre of the second scatterer over the one at the rim;  $\lambda$  is the only free parameter of the model. The value of  $\sigma_\theta(1)$  is obtained from the incident energy and NeT; the angular divergence of the beam at nozzle entrance is (currently) assumed to be 0.

It is not difficult to prove that, given the aforementioned rules for generating the  $(y, \theta)$  events, the open-field fluence at a lateral position  $y$  at depth  $z < \text{SAD}$  is given by

$$f(y) = \frac{R_L}{2\pi\sigma_s(\text{SAD} - z)} \int_{-1}^{t_0} \frac{dt}{\sigma_\theta(t)} \exp\left(-\frac{t^2 R_L^2}{2\sigma_s^2}\right) \exp\left(-\frac{\left(\frac{y-tR_L}{\text{SAD}-z} - \frac{tR_L}{L}\right)^2}{2\sigma_\theta^2(t)}\right), \quad (10)$$

where  $t_0 = 1$ . It has to be emphasised that this definition of the fluence does not involve an overall  $\frac{1}{r^2}$ -factor ( $r$  being the distance between the calculation plane and

the source); therefore, this formula is compatible with the format in which the lateral fluence measurements, used during the beam-configuration phase, appear.

It can be shown that the only modification in case that a half-block is inserted into the beamline (e.g., as shown in Fig. 1) involves the upper limit  $t_0$  of integration in Eq. (10); instead of  $t_0 = 1$ , one must now use

$$t_0 = \min \left\{ \frac{b(\text{SAD} - z) - y(\text{SAD} - \text{IBD})}{R_L(\text{IBD} - z)}, 1 \right\} \quad (11)$$

if  $t_0 > -1$ , or otherwise  $t_0 = -1$ .

Although the method of the present paper was originally developed for the double-scattering technique, it is also applicable in single scattering and uniform scanning; in both cases, one simply has to fix the parameter  $\lambda$  to 1. As the method is applicable only in case of broad fields, it has no bearing on modulated scanning.

*2.3.3. Multiple scattering through small angles* The elements needed for the description of the passage of particles through matter may be found (in a concise form) in Yao *et al* (2006), starting on page 258; most of the deflection of a charged particle traversing a medium is due to Coulomb scattering off nuclei. Despite its incompleteness (e.g., see the discussion in the GEANT4 physics-reference manual, section on ‘Multiple Scattering’, starting on page 71), the multiple-scattering model of Molière is used here. The large-angle scattering is not taken into account; the angular distribution of the traversing beam is assumed Gaussian.

Highland’s logarithmic term, appearing in the expression of  $\theta_0$ , will be approximated by a constant factor involving the block thickness; a similar strategy was followed in Gottschalk *et al* (1993). The Lynch-and-Dahl (1991) values will be used in the expression for  $\theta_0$ :

$$\theta_0(q) = \frac{13.6 \text{ MeV}}{\beta c p} \sqrt{\frac{q}{X_0}} \left( 1 + 0.038 \ln\left(\frac{d}{X_0}\right) \right), \quad (12)$$

where  $q$  denotes the depth along the original trajectory,  $\beta c$  the velocity and  $p$  the momentum of the proton, and  $X_0$  the radiation length in the material of the block (for a convenient parameterisation of  $X_0$ , see Yao *et al* (2006), page 263).

Equation (12) applies to ‘thin’ targets. For ‘thick’ targets, the dependence of the proton momentum on the depth  $q$  must be taken into account. Omitting the logarithmic term on the right-hand side, one may put Eq. (12) in the form

$$\theta_0(q) = 2f(q)\sqrt{q}, \quad (13)$$

where

$$f(q) = \frac{13.6 \text{ MeV}}{2\sqrt{X_0}} \left( \frac{1}{q} \int_0^q \frac{dt}{(\beta(t)cp(t))^2} \right)^{1/2}. \quad (14)$$

On the practical side, Eq. (13) with a constant (or at least ‘not too complicated’)  $f(q)$  factor would be attractive as one would then be able to obtain fast analytical solutions for the propagation of a simulated track inside the material of the block. Therefore,

it is worth determining the range of thickness values within which the constancy of the  $f(q)$  factor remains a reasonable assumption. The direct comparison with the data of Gottschalk *et al* (1993) revealed that the ‘thick-target’ corrections are unfortunately indispensable at depths exceeding about 50% of the range of 158.6-MeV protons, incident on a variety of materials.

To abide by the original goal of obtaining a fast solution, we had to follow an alternative approach (to that of using Eq. (14)), by parameterising the  $q$ -dependence of the  $f(q)$  factor in a simple manner; at present, the best choice seems to be to make use of the empirical formula

$$\theta_0(q) = \frac{2f\sqrt{q}}{1 - \frac{q^2}{1.75R^2}}, \quad (15)$$

where  $R$  denotes the (energy-dependent) range of the incident proton in the material of the block and

$$f = \frac{13.6\text{MeV}}{\beta cp} \frac{1}{2\sqrt{X_0}} \left(1 + 0.038 \ln\left(\frac{d}{X_0}\right)\right); \quad (16)$$

$f$  is now a constant, depending only on the initial value of  $\beta$ . The validation of Eqs. (15) and (16) was made on the basis of a comparison with the experimental data of Gottschalk *et al* (1993), namely the measured  $\theta_M$  values of that paper. Good agreement with the data was obtained for four materials which are of interest in the context of the present study (carbon, lexan, aluminum, and lead). Only at one entry (one of the largest depth values in lead, i.e., the measurement at  $q/R = 0.97548$ ), was a significant difference (of slightly less than 20%) found; the origin of that difference was not sought.

*2.3.4. Details on the generation of the MC events* Figure 10 shows an example of a trajectory of one proton inside a block. The incident proton, an OT in this figure, hits the upstream face of the block at angle  $\theta$  with respect to the beam axis. Two new *in-plane* variables are introduced to describe the kinematics at depth  $q$  (along the direction of the original trajectory): the deflection  $r$  (off the original-trajectory course) and the angle  $\phi$  (with respect to the direction of the original trajectory). Although the proton moves in an irregular path inside the block, the ‘history’ of the actual motion will be replaced by a smooth movement leading to the same value of  $r$  at  $q$ . This ‘smooth-deflection’ approximation will enable the association of the energy loss in the material of the block with the doublet of  $(q,r)$  values. Since the path length, which is calculated in this approximation, is an underestimate of the actual path length, a constant § conversion factor (true-path correction) of 0.9 has been used; there is some arbitrariness concerning this choice, yet it appears to be reasonable. It needs to be stressed that, in Fig. 10,  $x$  denotes the direction of the beam propagation; the auxiliary coordinate system introduced in this figure should not be confused with the coordinate system of Fig. 6, which is the formal one in medical applications.

§ In reality, the true-path correction is expected to be energy-dependent.

In the generation of the MC events, the suggestion of Yao *et al* (2006), page 262, for the quantities  $r$  and  $\phi$  has been followed. Two independent Gaussian random variables  $(z_1, z_2)$  with mean 0 and variance 1 are first created in each event (track hitting the block). The quantities  $r$  and  $\phi$  are expressed in terms of  $(z_1, z_2)$  as follows:

$$r(q) = \left( \frac{z_1}{\sqrt{3}} + z_2 \right) \frac{q\theta_0(q)}{2} \quad (17)$$

and

$$\phi(q) = z_2\theta_0(q), \quad (18)$$

where  $\theta_0(q)$  is taken from Eq. (15).

The values of the doublet  $(z_1, z_2)$  fix the dependence of  $r$  and  $\phi$  on  $q$  in each generated event. It may then be determined (either analytically or numerically) whether the particular track leaves the block. Finally, for those tracks leaving the block, a simple rotation yields the coordinates of the exit point in the  $(x, y)$  coordinate system of Fig. 10. The energy of the leaving proton is determined from its residual range (original range minus the actual path length inside the material of the block).

*2.3.5. The lateral fluence distributions of the scattered protons* The definitions of the three types of scattered protons have been given in Section 1; in Fig. 1, one obtains a rough schematic view of the corresponding contributions to the fluence. In this section, we will introduce convenient forms to parameterise the lateral fluence distributions of the scattered protons.

As far as these distributions are concerned, the uninteresting offset  $b$  (lateral displacement of the block) in Fig. 1 will be omitted. Therefore, for the needs of this section,  $y = 0$  mm at the extension of the block in Fig. 1, that is, not at the position where the central beam axis intersects the calculation plane. To obtain the lateral fluence distributions, literally corresponding to Fig. 1, one has to take the offset  $b$  into account. In the formulae below, the placement of the half-block is assumed as shown in Fig. 1 (i.e., extending to  $+\infty$ ).

The empirical formula for the description of the lateral fluence distribution of the OTs reads as

$$f(y) = \alpha \exp(-y/\beta) (y + \gamma)^2, \quad (19)$$

where  $y \leq 0$ . Four conditions for the parameters  $\alpha$ ,  $\beta$ , and  $\gamma$  must be fulfilled:  $\alpha > 0$ ,  $\beta < 0$ ,  $\gamma \leq 0$ , and  $2\beta - \gamma \leq 0$ .

The same empirical formula is used in the parameterisation of the lateral fluence distribution of the BSITs; the four aforementioned conditions also apply. (The resulting optimal parameter values are, of course, different.)

The optimal description of the (broader distribution of the) GTITs is achieved on the basis of a Lorentzian

$$f(y) = \frac{\alpha\gamma^2}{(y - \beta)^2 + \gamma^2}, \quad (20)$$

multiplied by the asymmetry factor

$$\frac{2}{1 + \exp(-2\frac{y-\beta}{\gamma})},$$

to account for the observed skewness of the lateral fluence distribution (toward positive  $y$  values). Three conditions must be fulfilled:  $\alpha > 0$ ,  $\beta \geq 0$ , and  $\gamma > 0$ .

The lateral fluence distribution of the pristine tracks is fitted by using the standard formula

$$f(y) = \alpha \left(1 - \Phi\left(\frac{y - \beta}{\gamma}\right)\right), \quad (21)$$

where  $\alpha > 0$  and  $\gamma > 0$ ;  $\Phi(x)$  is the cumulative Gaussian distribution function. Only the factor  $\alpha$  will be retained from the fits to the pristine-beam data, to be used in the *normalisation* of the fluence corresponding to each of the three types of scattered protons. Expressing the contributions of the scattered protons as fractions of the pristine-beam fluence enables the efficient application of the corrections at planning time.

From all the above, it is evident that the description of the contribution to the fluence (at fixed  $z$ ) of any of the three types of the scattered protons is achieved on the basis of three parameters; hence, there are nine parameters in total. At the end of each cycle (comprising a set of MC runs for a number of  $b$  values, for a given energy-NeT combination), each of these nine parameters  $p_i$  is expanded in terms of  $b$  and  $z$ , using the quadratic model

$$p_i = a_{i1} + a_{i2}b + a_{i3}z + a_{i4}bz + a_{i5}b^2 + a_{i6}z^2. \quad (22)$$

The final results are the 56 coefficients  $a_{ij}$ ,  $i \in \{1, \dots, 9\}$ ,  $j \in \{1, \dots, 6\}$ , obtained at several energy-NeT combinations for the option of the machine which is under calibration. At planning time, the values of the parameters  $p_i$  are reconstructed from the existing results (via simple 2D interpolations in the incident energy and NeT), the values of  $b$  (corresponding to the particular miniblock which is processed), and  $z$  (corresponding to the calculation plane which is processed).

*2.3.6. A summary of the approach* Let us assume that one option of a selected machine has been chosen for calibration (at beam-configuration phase). All half-block data (which is contained in that option) is used in the determination of the parameter  $\lambda$  on the basis of an optimisation scheme (featuring the C++ implementation of the standard optimisation package MINUIT of the CERN library), along with Eq. (10) with the  $t_0$  value of Eq. (11) ||.

Representative incident-energy and NeT values are chosen from the ranges of values associated with the option which is under calibration. For each acceptable energy-NeT

|| For the determination of the parameter  $\lambda$ , one could also use the measurements of the open-field fluence, along with Eq. (10) with  $t_0 = 1$ . However, what is habitually called ‘open-field measurements’ in the field of radiation therapy corresponds to beams which have already been restricted in size by the primary collimator.

combination, a number of MC runs are performed, each corresponding to one  $b$  value. In each of these MC runs, events (i.e.,  $(y, \theta)$  pairs, each corresponding to one proton track) are generated according to the formalism developed in Section 2.3.2. The value of the parameter  $\lambda$ , obtained from the half-block data (for the option in question) at the previous step, comprises (i.e., apart from geometrical characteristics of the machine which is configured) the only input to these MC runs. The resulting tracks are followed until they either hit the block or pass through it. The tracking of the protons inside the material of the block is done according to Section 2.3.4; finally, these tracks either vanish (being absorbed in the material of the block) or emerge from it (bore, downstream face) and deliver dose.

The tracks which emerge from the block are properly flagged (OTs, BSITs, or GTITs) and their contributions to the fluence at a number of  $z$  depths are stored (histogrammed). Fits to these distributions, using the empirical formulae of Section 2.3.5, lead to the extraction of the parameters achieving the optimal description of the stored data. After the completion of all the runs for all the chosen values of  $b$ , the entire set of the parameter values is subjected to fits by using Eq. (22) for each parameter separately. Finally, the coefficients  $a_{ij}$ ,  $i \in \{1, \dots, 9\}$ ,  $j \in \{1, \dots, 6\}$ , appearing in Eq. (22), are stored in files along with the values of the incident energy and NeT corresponding to the particular MC run; these output files will comprise the only input when the corrections to a particular plan will be derived (planning time).

The procedure above is repeated until all options of the given proton-treatment machine have been calibrated. The variability in the material and in the thickness of the block is also taken into account in the current implementation (by looping over those combinations requested by the user ¶). Finally, it is worth repeating that this time-consuming part of obtaining the files containing the  $a_{ij}$  coefficients (a question of a few hours per option) has to be performed only once, when the proton-treatment machine is configured.

At planning time, the pristine-beam fluence is calculated first. The beam-scattering corrections are then obtained (i.e., if they have been requested) after employing a number of elements developed in the course of the present section:

- The concept of miniblocks introduced in Section 2.1.
- The reconstruction of each of the nine parameters, used in the description of the scattered protons, at a few  $z$  values, on the basis of Eq. (22) from the results pertaining to the option selected in the treatment plan. The appropriate file (corresponding to the block material and thickness in the plan) is used as input. The final results for the various parameters are obtained via simple 2D interpolations in the incident energy and NeT.
- The empirical formulae of Section 2.3.5.

¶ At present, five materials are supported: brass, cerrobend, nickel, copper, and lead; this list is easily expandable. The block-thickness values are taken from the option properties of the machine which is configured.

- A simple (linear) interpolation to obtain the corrections at all depths  $z$  in the plan.

The final step involves the application of the corrections to the pristine-beam fluence.

The break-up of the task of determining the scattering corrections into two steps, as described in this section of the paper, enables the minimisation of the time consumption during the evaluation and application of these corrections in proton planning; of central importance, in this respect, is the concept of miniblocks.

### 3. Results

#### 3.1. Machine configuration

The measurements, which are analysed in this paper, have been obtained at the Proton Therapy Centre of the National Cancer Centre (NCC), South Korea. The first report on the clinical commissioning and the quality assurance for proton treatment at the NCC appeared slightly more than one year ago, see Lee (2007).

The NCC proton-treatment machine has been manufactured by Ion Beam Applications (IBA), Louvain-la-Neuve, Belgium. Its nominal SAD is 2300 mm and the distance between the first scatterer and the isocentre is 2792 mm. The double-scattering technique currently supports eight options with incident energies ranging from 155 to 230 MeV.

*3.1.1. Half-block fluence measurements* All half-block measurements have been taken in air, using  $IBD = 250$  mm. The lateral displacement of the 65mm-thick brass block, used in these measurements, was  $b = -50$  mm; the block was positioned opposite to what is shown in Fig. 1, i.e., blocking to beam from  $-50$  mm to (theoretically)  $-\infty$ . To apply Eq. (10) with the  $t_0$  value of Eq. (11), the  $y$  axis was inverted, as a result of which the  $b$  value of  $+50$  mm was finally used in Eqs. (10) and (11). Each option of the double-scattering technique at the NCC comprises 15 energy-NeT combinations; in each of these combinations, the lateral fluence distributions have been obtained at four  $z$  positions, namely at  $z = -300, -150, 0,$  and  $150$  mm. One example of these profiles is given in Fig. 11. It is worth mentioning that each profile had been separately normalised (during the data taking) by setting the corresponding average value of the fluence ‘close’ to the central beam axis to (the arbitrary value of)  $100^+$ ; unfortunately, the individual normalisation factors are not available. The ‘ears’ of the distribution for the data set at  $z = 150$  mm, which are presumably due to block scattering, have been

<sup>+</sup> At present, the analysis of the half-block fluence measurements is tedious. Unfortunately, there is no standard format in which these measurements, taken at the various treatment centres and machines, have to appear; in fact, there is complete freedom (during machine configuration) in the choice of the distance between the downstream face of the block and the isocentre, in the thickness and the lateral displacement of the block, and in the normalisation factors used in the output files. A more serious drawback is that the measurements are frequently (luckily, not in the NCC case) shifted laterally, so that the 50% of the corresponding maximal fluence (of each set, separately) be brought to  $y = 0$  mm; thus, an important offset is irretrievably lost.



removed via software cuts. To avoid fitting the noise, fluence values below 10% of the maximal value in each data set were not processed. The block-thickness effects were removed from the data prior to processing.

Before advancing to the results, one important remark is prompt. A significant deterioration of the description of the data in the last of the options (option 8) was discovered during the analysis; at present, it is not entirely clear what causes this problem. It seems that our beamline model leads to a systematic overestimation of the penumbra in option 8. It has to be mentioned that the data in that option yields an unusually small spot size ( $\sigma_s$ ), about 3 times smaller than the typical values extracted in the other seven options. Option 8 is the only one in which the IBA second scatterer SS<sub>3</sub> (which is admittedly of peculiar design \*) is used. In all probability, the problems seen in option 8 originate from the shape of the second scatterer, namely from the fact that the energy loss in its material is not kept constant radially (actually, it is ‘discontinuous’ at  $t \sim 0.9$ ). In order to investigate the sensitivity of our conclusions to the treatment of option 8, we will perform the analysis both including in and excluding from the database the measurements of that option.

*3.1.2. Extraction of parameter  $\lambda$*  The extracted values of the parameter  $\lambda$  for all the energy-NeT combinations of all double-scattering options of the NCC machine are shown in Fig. 12. The uncertainties in the case of option 8 are (on average) larger than in the other options. The variability of the values within each option is due to the fact that, as a result of the numerous assumptions made to simplify the problem,  $\lambda$  (which should, in principle, characterise only the second scatterer) was finally turned into an effective parameter. To decrease the ‘noise’ seen in Fig. 12, the weighted average of the extracted  $\lambda$  values within each option was finally used in the ensuing MC runs for all energy-NeT combinations in that option (see Table 1).

*3.1.3. Monte-Carlo runs* 50 million events have been generated in each energy-NeT combination, at each of three  $b$  values (20, 40, and 60 mm). The lateral fluence distributions have been obtained at 17 positions in depth, from  $z = 100$  to  $-100$  mm. The parameters of these distributions for the three types of scattered protons have been extracted using the formulae of Section 2.3.5. In all cases (i.e., including option 8), the description of the data was good; the reduced  $\chi^2$  values ( $\chi^2/\text{NDF}$ , NDF being the number of degrees of freedom in the fit) came out reasonably close to 1. Figures 13 and 14 show typical lateral fluence distributions for outer and inner tracks, respectively.

\* The amount of lead, used at the centre of the SS<sub>3</sub>, is smaller than in the cases of the SS<sub>8</sub> and SS<sub>2</sub> scatterers which are used in options 1-7. Furthermore, the thickness of lexan *abruptly* increases close to the rim of this scatterer. Evidently, the amount of material used in the SS<sub>3</sub> cannot provide efficient broadening of the beam; adding material would imply smaller beam energy at nozzle exit, at a time when the emphasis in this option is obviously put on the high end of the energy spectrum. To be compatible with the requirement for flatness of the resulting field at isocentre, a smaller maximal field diameter (140 versus 220 to 240 mm of the other options) in the clinical application of option 8 had to be imposed.

Figures 15-17, obtained with a lateral block displacement of  $b = 20$  mm, show the scattering corrections (to be applied to the lateral fluence distributions of the pristine tracks) at three  $z$  positions around the isocentre (100, 0, and  $-100$  mm, respectively). As expected, the distributions broaden when receding from the block; the mode of the fluence contribution of the OTs moves about 1 mm away from the block extension for every 10 mm of depth, thus indicating an ‘average’ exit angle (to the bore) of about  $6^\circ$ . Concerning their magnitude, the corrections generally amount to a few percent of the corresponding pristine fluence for the typical distances involved in clinical applications.

It is now time to enter the subject of the energy loss of the scattered protons. To a good approximation, one may assume that the energy distributions of the scattered protons depend only on the ratio  $\omega = E/E_{\max}$ , where  $E$  is the energy of the scattered proton and  $E_{\max}$  denotes the energy of the pristine beam (i.e., the energy at nozzle exit). In their study, Kimstrand *et al* (2008) made the same observation. The energy distributions of the scattered protons were investigated in the case of three energy-NeT combinations of the NCC machine: (158.42 MeV, 125.3 mm), (182.99 MeV, 65.6 mm), and (229.75 MeV, 40.7 mm). These combinations have been selected from the data sets of options 1, 5, and 8, respectively, in which different second scatterers are employed; the corresponding energies  $E_{\max}$  are: 79.5, 150.2, and 212.8 MeV. The results have been obtained using a 65-mm thick brass block. Figures 18 and 19 show the energy distributions of the scattered protons as functions of the ratio  $\omega$ ; instead of referring explicitly to each energy-NeT combination, we will simply use the option number (or  $E_{\max}$ ) to identify the results. The following remarks are worth making.

- At low and moderate values of the exit energy  $E_{\max}$ , the energy distributions of the two types of inner tracks are similar, following the  $f(\omega) = 2\omega$  probability distribution. At the high end of the energies used in the NCC machine, the energy distribution of the BSITs departs from this simplified picture, attaining a peak close to  $\omega = 1$ ; this is due to BSITs which almost ‘brush’ the surface of the bore. The energy distribution of the GTITs remains unchanged. Nevertheless, to retain simplicity, we will assume that the energy distribution of all inner tracks follows the formula  $f(\omega) = 2\omega$ .
- The energy distribution of the OTs is strongly smeared toward low  $\omega$  values. The OTs lose a significant amount of their energy when traversing the material of the block; as shown in Fig. 18, their energy distributions peak around  $\omega \sim 0.2$  to  $0.3$ . To fit the energy distribution of the OTs, we used the empirical formula

$$f(\omega) \sim \sqrt{\omega} \exp(-\eta\omega),$$

where the parameter  $\eta$  turns out to be around 2 to 2.5; the constant of proportionality is obtained from the normalisation of the probability distribution.

Courant’s effective-size corrections, corresponding to the three aforementioned cases, are: 0.31, 0.87, and 1.57 mm. At small aperture sizes, the dominant contribution to the fluence (of the scattered protons) originates from OTs; the inner tracks dominate

at high aperture values. The crossover is energy-dependent, ranging from about 15 (option-1 result) to 47 mm (option-8 result).

The absolute yields of the different types of the scattered protons are given in Table 2 for an aperture size (i.e., the diameter, assuming circular shape) of 100 mm. We observe that the absolute yield of the OTs increases by a factor of about 2 between 79.5 and 150.2 MeV, and by more than 4 between 150.2 and 212.8 MeV. At 79.5 MeV, the BSITs account for more than 50% of the total yield of the scattered protons. However, the importance of the BSITs diminishes with increasing energy, reaching the level of 1 out of 4 OTs at 212.8 MeV. On the contrary, the yield of the GTITs flattens out at about 0.75 per OT. One might conclude that the BSITs seem to be more important at low energies and the OTs at high energies. The ratio of the yields of the GTITs and OTs is almost constant, varying only from 2/3 to 3/4 as the energy increases from 79.5 to 212.8 MeV.

### 3.2. Verification of the method

The verification of the method of the present paper should obviously involve the reproduction of dedicated dose measurements obtained in some material which, as far as the stopping power for protons is concerned, resembles human tissue, e.g., in water. The measurements should cover the region around the isocentre, where the tumour is usually placed, and, in order that the approach be validated also in the entrance region, they should extend to small distances from (the downstream face of) the block. Finally, the method must be validated for a range of depth values (associated with the energy at nozzle exit).

At present, given the lack of dedicated dose measurements, the only possibility for verification rests on re-using the calibration data (i.e., the half-block fluence measurements described in Section 3.1.1). We are aware of the fact that using the same data for configuring a system and for validating its output does not constitute an acceptable practice. However, since parts of the data (i.e., the areas which are obviously contaminated by the block-scattering effects) had been removed from the database before extracting the  $\lambda$  values, this approach becomes a valid option. Luckily, as far as the validation of the scattering corrections to the fluence is concerned, our interest lies in (the reproduction of) those excluded areas; naturally, for the rest of the measurements (i.e., for those which *were* used in the determination of the  $\lambda$  values), it has to be verified that the quality of the description of the experimental data is not impaired by the inclusion of the block-scattering corrections.

A typical reproduction of the measurements is given in Figs. 20 and 21; the data correspond to the first energy-NeT combination of option 1 of the NCC machine, taken at  $z = 150$  mm (i.e., 100 mm away from the block). Shown in Fig. 20 are the lateral fluence measurements (continuous line) along with the MC data corresponding only to the pristine beam; the effects of the scattered protons are added to the pristine-beam fluence (resulting in what will be called henceforth ‘total fluence’) in Fig. 21. On the

basis of the visual inspection of these two figures, there is no doubt that the quality of the reproduction of the measurements in the latter case (i.e., when including the block-scattering effects) is superior.

We will next investigate the goodness of the reproduction of all measurements on the basis of a commonly-used statistical measure, e.g., of the standard  $\chi^2$  function. Alternative options have been established (e.g., the  $\gamma$ -index approach of Low *et al* (1998)), but have not been tried in this work. One has to bear in mind that the block-scattering contributions are larger at small distances from the block and in the area neighbouring its extension; at large distances, the distributions of the scattered protons broaden as a result of the angular divergence of the scattered beam and, less importantly, of scattering in air (an effect which has not been included in this paper). Evidently, the assessment of the goodness of the reproduction of the data, paying no attention to the characteristics of the effect in terms of the depth  $z$ , makes little sense.

The measurements in the area corresponding to the penumbra are very sensitive to the (input) value used for the lateral displacement of the block; small inaccuracy in this value affects the description of the data significantly, introducing spurious effects in the  $\chi^2$  function. This area, albeit very important in the determination of the value of the parameter  $\lambda$ , was not included in this part of the analysis.

The resulting  $\chi^2$  values are given in Table 3, separately for the four  $z$  positions at which the measurements have been obtained; it is evident that, for all depth values, the quality of the reproduction of the measurements when including the block-scattering effects is superior to the case that only the pristine-beam contribution is considered. The importance of the inclusion of these effects decreases with increasing distance to the block. The improvement for  $z = 150$  mm when including the block-scattering effects is impressive. Judging from the  $\chi^2$  values for the given degrees of freedom, there can be no doubt that the overall reproduction of the data is satisfactory. Last but not least, despite the fact that the description of the option-8 measurements is debatable, our conclusions do not depend on the treatment of the data in that option (i.e., inclusion in or exclusion from the database).

Out of the available 120 lateral fluence profiles, corresponding to  $z = 150$  mm, only five profiles did not show improvement after the scattering effects were included. In two of these profiles, namely the energy-NeT combinations of (176.08 MeV, 102.2 mm) and (179.00 MeV, 103.3 mm), the scattering contributions are present in the measurements, yet at different amounts compared to the MC-generated data; additionally, a hard-to-explain slope (i.e., of different sign to what is expected after including the scattering contributions) is clearly seen in these measurements around  $y = 0$  mm. On the other hand, no scattering effects ('ears') are discernible in the (167.42 MeV, 160.5 mm), (206.77 MeV, 75.2 mm), and (204.47 MeV, 203.2 mm) combinations at  $z = 150$  mm. It has to be stressed that these five data sets are surrounded by a multitude of measurements showing an impressive agreement between the experimentally-obtained and the MC-generated total-fluence distributions; due to this reason, we rather consider the absence of improvement (that is, after the scattering contributions are included) in

the description of the data in these five profiles as indicative of experimental problems.

An alternative way of displaying the content of Figs. 20 and 21 is given in Fig. 22; instead of showing separately the measurements and the MC data, shown in Fig. 22 are the normalised residuals, defined as

$$Z_i = \frac{v_i^{\text{MC}} - v_i^{\text{exp}}}{\sqrt{(\delta v_i^{\text{MC}})^2 + (\delta v_i^{\text{exp}})^2}},$$

where  $v_i^{\text{exp}}$  denotes the  $i$ -th measurement and  $v_i^{\text{MC}}$  the corresponding MC-obtained fluence;  $\delta v_i^{\text{exp}}$  and  $\delta v_i^{\text{MC}}$  represent their uncertainties. The advantage of such a plot is evident as direct information on the reproduction may be obtained faster than from Figs. 20 and 21; for instance, not only can one immediately become aware of the failure of the pristine-beam data close to the borders of the block, but also of the severity of this failure. Evidently, the pristine-beam contribution underestimates the fluence by about 1 to 3 standard deviations for  $-50 \text{ mm} < y < -40 \text{ mm}$ . It is also interesting to note that, after the scattering effects have been included, the normalised residuals  $Z_i$  show significantly smaller dependence on the lateral distance  $y$  (ideally, no dependence should be seen).

### 3.3. An example of the application of the corrections

The aim of the present paper was to provide the systematic description of a method to be used in the determination and application of the corrections which are due to the presence of BL/BSDs in proton planning. Despite the fact that no emphasis was meant to be put on a clinical investigation, one simple example (of the application of the corrections) may nevertheless be called for.

To this end, the current version of the Treatment Planning System Eclipse<sup>(TM)</sup> (Varian Medical Systems Inc., Palo Alto, California) was extensively modified to include the derivation (in beam configuration) and the application (in planning) of both block-relating corrections; the application of each of the two corrections may be requested separately in the user interface. (A review article, providing the details of the dose evaluation in proton therapy, as well as its implementation in Eclipse, will appear soon, see Ulmer *et al* (2009).) A simple rectangular water phantom was created, within which a planning treatment volume (PTV) of  $90 \text{ cm}^3$  was arbitrarily outlined. Four one-field treatment plans were subsequently created as follows:

- a) a plan without block-relating corrections,
- b) a plan with block-thickness corrections,
- c) a plan with block-scattering corrections, and
- d) a plan with both block-relating corrections ‡.

‡ To void double counting in the case that both block-relating corrections are requested, the block-thickness corrections are first applied to the pristine-beam fluence. The block-scattering corrections, which already contain their corresponding block-thickness effects, are subsequently added to the ‘thickness-corrected’ pristine-beam fluence.

In each of these plans, a brass block was inserted and fitted to the cross section of the PTV. Subsequently, a dose of 100 Gy was delivered to the PTV, using the double-scattering technique of the NCC machine. The block-relating corrections were estimated on the basis of  $N = 64$ ; in fact, the results are practically insensitive to the value of  $N$ , for  $N \geq 16$ . Finally, the resulting dose maps were compared; the dose differences of plans (b), (c), and (d) to plan (a) were estimated and compared (Figs. 23 and 24), leading to the following conclusions.

- As expected, the application of the block-thickness corrections results in lower dose values. This is due to the fact that part of the incident flux is blocked as a result of the nonzero thickness of the block.
- As expected, the application of the block-scattering corrections leads to higher dose values. This is because some protons, which would otherwise fail to contribute to the fluence (as they impinge upon the block), scatter off the material of the block and ‘re-emerge’ at positions in the bore or on the downstream face of the block.
- As far as the delivered dose is concerned, the effects of the block thickness and block scattering ‘compete’ one another. In the water phantom used in this section, the block-thickness corrections dominate.
- The presence of the block in the plan of the water phantom used in this section induces effects which amount to a few percent of the prescribed dose (see Fig. 24). The largest effects appear in the area neighbouring the border of the block. It is also worth noticing the characteristic contributions of the scattered protons in the entrance region in the frontal and sagittal views in Fig. 24; the largest part of the dose in the entrance region corresponds to the low-energy component of the scattered beam. As the *local* dose, delivered in the entrance region, is significantly smaller than the corresponding value delivered to the target (which, in fact, is an argument in favour of the use of protons in radiation therapy), the corrections which one has to apply to it, though representing a small fraction of the *prescribed* dose, are sizable.

#### 4. Conclusions

The present work deals with corrections which are due to the presence of beam-limiting and beam-shaping devices in proton planning. The application of these corrections is greatly facilitated by decomposing the effects of two-dimensional objects into one-dimensional, easily-calculable contributions (miniblocks).

In the derivation of the thickness corrections, we follow the strategy of Slopsema and Kooy (2006). Given the time restrictions during the planning, the derivation of the scattering corrections necessitates the introduction of a two-step approach. The first step occurs at the beam-configuration phase. At first, the value of the only parameter of our model ( $\lambda$ ) is extracted from the half-block fluence measurements. A number of Monte-Carlo runs follow, the output of which consists of the parameters pertaining

to convenient parameterisations of the fluence contributions of the scattered protons. These runs take account of the variability in the block material and thickness, incident energy, and nozzle-equivalent thickness in all the options for which a proton-treatment machine is configured. To enable the easy use of the MC results, the output is put in the form of expansion parameters in two geometrical quantities which are involved in the description of the scattering effects. The scattering corrections for all the blocks in a particular plan are determined from the results, obtained at beam-configuration phase, via simple interpolations.

The verification of the method should involve the reproduction of dedicated dose measurements. At present, given the lack of such measurements, the only possibility for verification rested on re-using the half-block fluence measurements, formerly analysed to extract the  $\lambda$  value; this is a valid option because parts of the input data had been removed from the database to suppress the (present in the measurements) block-scattering contributions. We investigated the goodness of the reproduction of the measurements on the basis of the  $\chi^2$  function and concluded that the inclusion of the scattering effects leads to substantial improvement.

The method presented in this paper was applied to one plan involving a simple water phantom; the different contributions from the two block-relating effects have been separately presented and compared. These effects amount to a few percent of the prescribed dose and are significant in the entrance region and in the area neighbouring the border of the block.

## Acknowledgments

The author acknowledges helpful discussions with Barbara Schaffner concerning the optimal implementation of the method in Eclipse. Barbara also modelled and implemented in Eclipse the important (in the entrance region) dose contributions of the low-energy scattered protons (i.e., those with energies below the lowest value used in the particular plan to ‘spread out’ the Bragg peak). The author is grateful to Se Byeong Lee for providing the original NCC half-block fluence measurements, as well as important information on the data taking.

## References

- Burge E J and Smith D A 1962 Theoretical Study Of Slit Scattering *Rev. Sci. Instrum.* **33** 1371
- Courant E D 1951 Multiple Scattering Corrections for Collimating Slits *Rev. Sci. Instrum.* **22** 1003
- Geant4, Physics Reference Manual, version: geant4 9.1 (14 December, 2007); available from the internet address <http://geant4.web.cern.ch/geant4/support/userdocuments.shtml>
- Gottschalk B, Koehler A M, Schneider R J, Sisterson J M and Wagner M S 1993 Multiple Coulomb scattering of 160 MeV protons *Nucl. Instr. Meth.* **B74** 467
- Highland V L 1975 Some practical remarks on multiple scattering *Nucl. Instr. Meth.* **129** 497
- ICRU Report 1987 Use of Computers in External Beam Radiotherapy Procedures with High-Energy Photons and Electrons **42** 1

- Kimstrand P, Traneus E, Ahnesjö A and Tilly N 2008 Parametrization and application of scatter kernels for modelling scanned proton beam collimator scatter dose *Phys. Med. Biol.* **53** 3405
- Lee S B 2007 Clinical Commissioning and Quality Assurance of Proton beam in NCC, Korea *PTCOG 46*; available from the internet address <http://ptcog.web.psi.ch/PTCOG46>
- Low D A, Harms W B, Mutic S and Purdy J A 1998 A technique for the quantitative evaluation of dose distributions *Med. Phys.* **25** 656
- Lynch G R and Dahl O I 1991 Approximations to multiple Coulomb scattering *Nucl. Instr. Meth.* **B58** 6
- Minuit2 Minimization Package, 5.20/00; available from the internet address <http://project-mathlibs.web.cern.ch/project-mathlibs/sw/Minuit2/html/index.html>
- Paganetti H 1998 Monte Carlo method to study the proton fluence for treatment planning *Med. Phys.* **25** 2370
- Slopesma R L and Kooy H M 2006 Incorporation of the aperture thickness in proton pencil-beam dose calculations *Phys. Med. Biol.* **51** 5441
- Takada Y 2002 Optimum solution of dual-ring double-scattering system for an incident beam with given phase space for proton beam spreading *Nucl. Instr. Meth.* **A485** 255
- Ulmer W, Matsinos E and Kaissl W 2009 Theoretical methods for the calculation of Bragg curves and 3D distributions of proton beams; to appear in *Radiation Physics and Chemistry*
- van Luijk P, van 't Veld A A, Zelle H D and Schippers J M 2001 Collimator scatter and 2D dosimetry in small proton beams *Phys. Med. Biol.* **46** 653
- Yao W-M *et al* 2006 The Review of Particle Physics *J. Phys.* **G33** 1; available from the internet address <http://pdg.lbl.gov/>



**Table 1.** The weighted averages of the extracted  $\lambda$  values (and their statistical uncertainties) for the eight options of the NCC machine. The uncertainties are shown only for the sake of completeness; they have not been taken into account in the results of Section 3.1.3.

Option number	$\lambda(\delta\lambda)$
1	4.667 (0.046)
2	5.020 (0.070)
3	4.549 (0.057)
4	4.857 (0.069)
5	4.800 (0.090)
6	5.26 (0.11)
7	6.42 (0.15)
8	4.65 (0.27)

**Table 2.** The absolute yields (numbers of particles) of the different types of the scattered protons for an aperture size of 100 mm, for three energy-NeT combinations of the NCC machine (see text); a 65-mm thick brass block has been used.

$E_{\max}$ (MeV)	OTs	BSITs	GTITs
79.5	35696	64130	23799
150.2	72015	42128	54383
212.8	319806	83808	242229

**Table 3.** The  $\chi^2$  values, corresponding to the reproduction of the half-block fluence measurements, separately for the four  $z$  positions at which the data have been obtained; evidently, the quality of the reproduction of the measurements when including the block-scattering effects is superior to the case that only the pristine-beam contribution is taken into account. NDF denotes the number of degrees of freedom. The lower part of the table contains the results after excluding the measurements of option 8.

$z$ (mm)	$\chi^2$ Pristine	$\chi^2$ Total	NDF
150	22710.25	8551.34	14511
0	15384.09	11826.71	14210
-150	13229.26	12255.67	13841
-300	12949.22	12573.03	13628
150	16024.44	5761.21	12704
0	12001.81	9761.32	12404
-150	10751.43	10277.58	12057
-300	10658.78	10531.18	11843

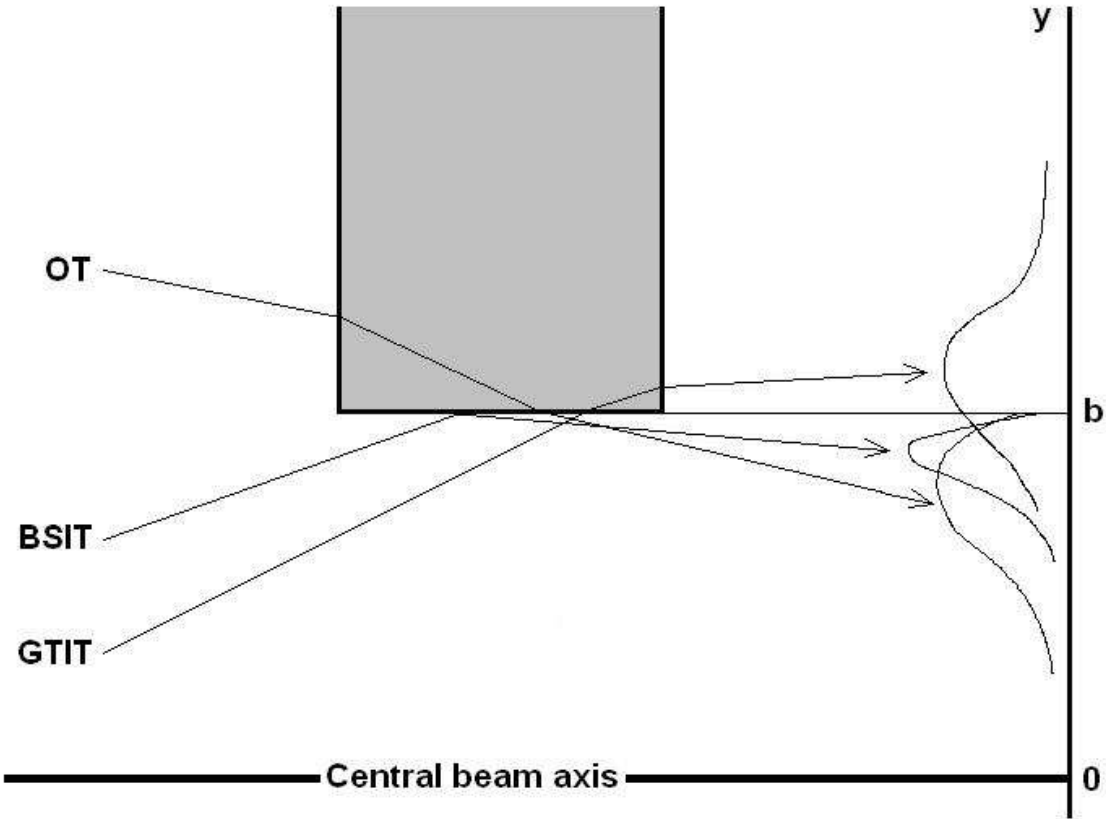


**Figure 1.** The outer tracks (OTs) and the bore-scattered inner tracks (BSITs) emerge from the bore. The going-through inner tracks (GTITs) emerge from the downstream face of the block.

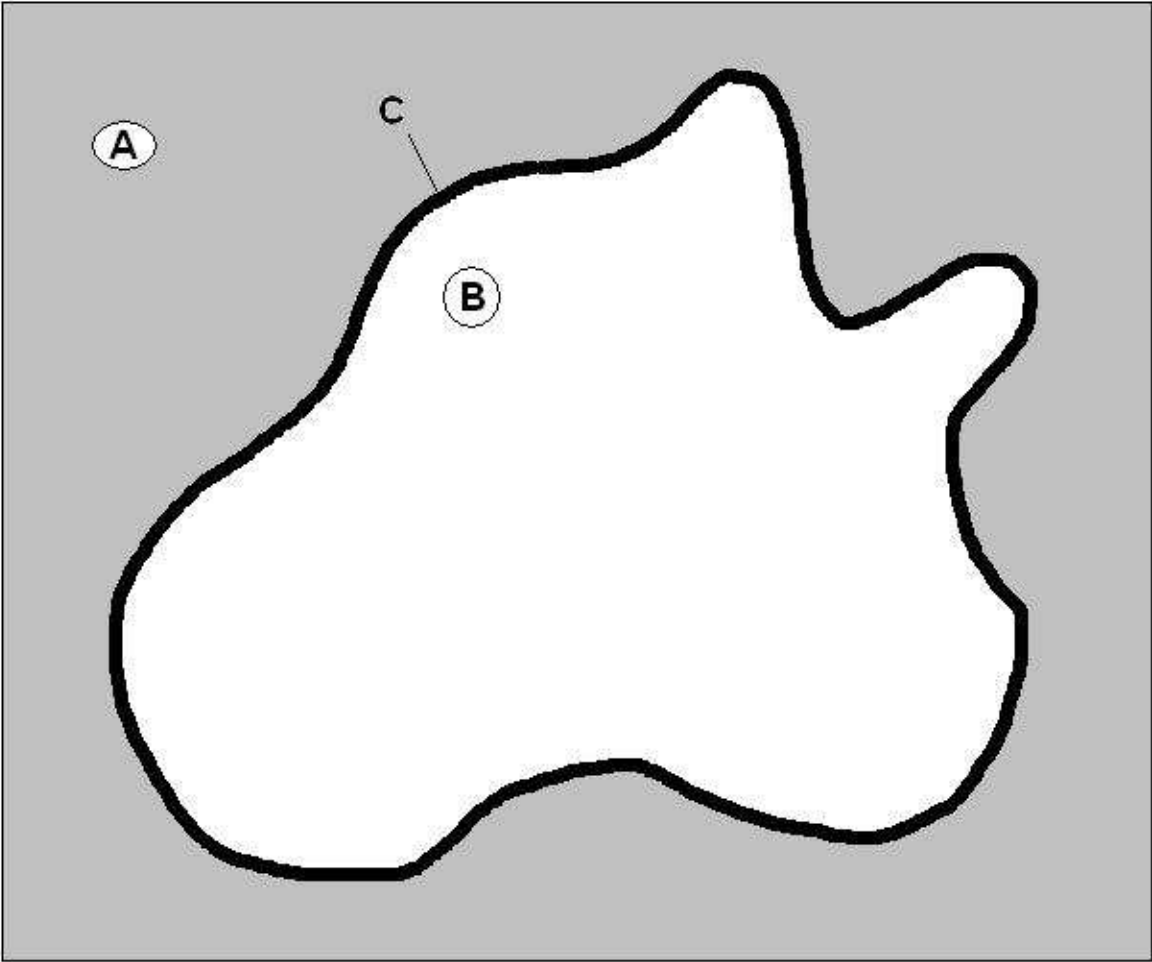
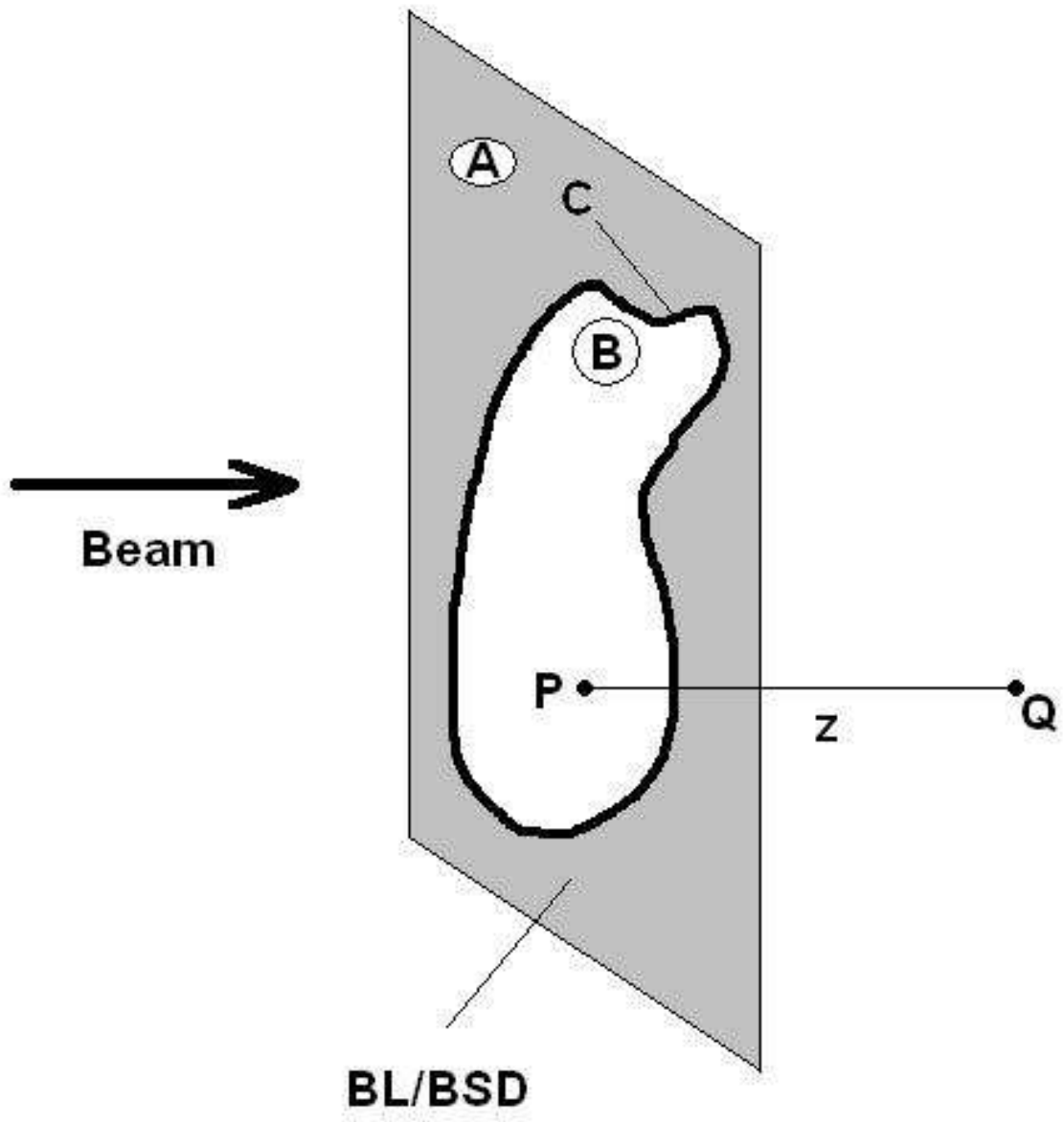
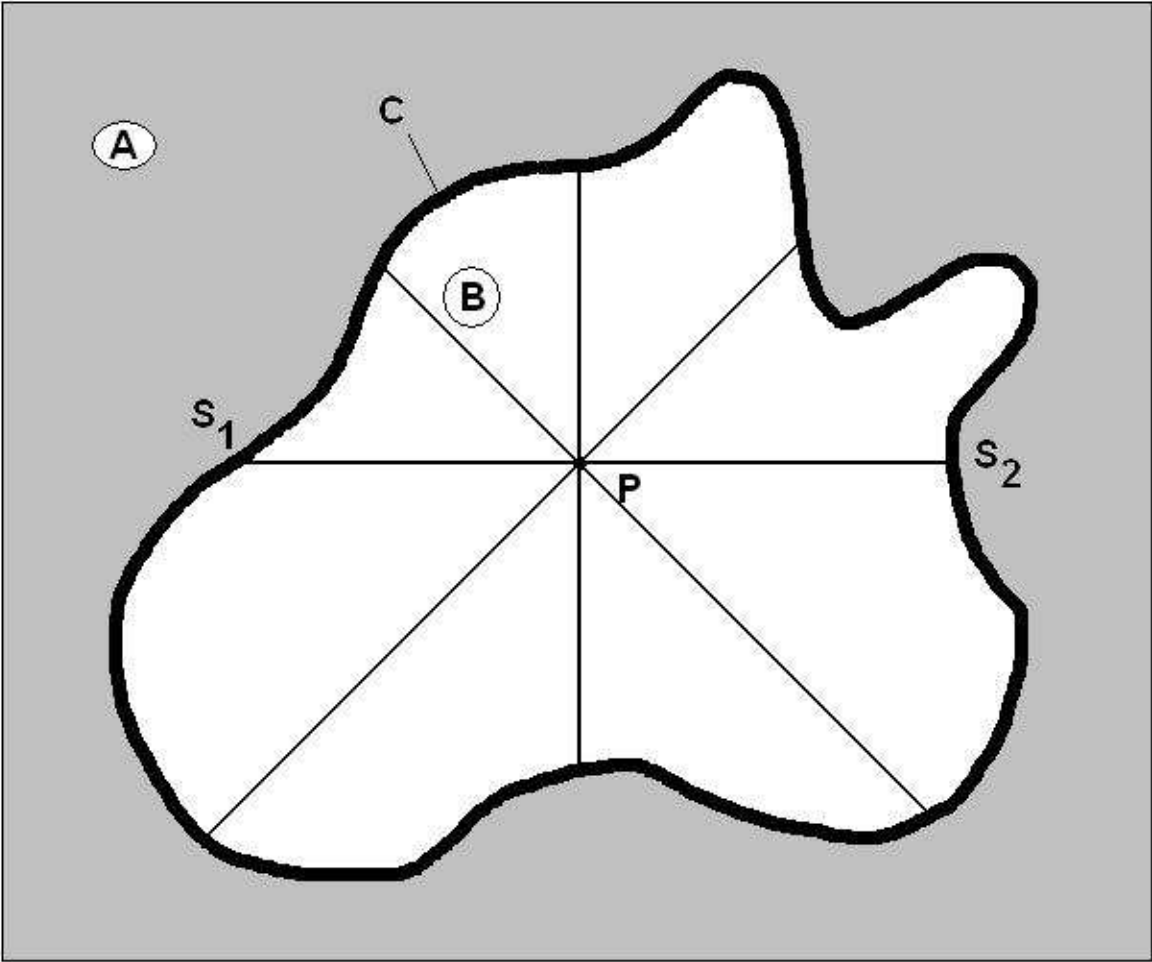


Figure 2. Example of a BL/BSD (reduced to two dimensions) in beam's eye view.



**Figure 3.** The effects of the BL/BSD have to be evaluated at the point Q, which is projected to the point P on the BL/BSD plane. In this figure, the point P lies within the area B.



**Figure 4.** Evaluation of the effects of the BL/BSD at the point Q of Fig. 3 (not shown), whose projection onto the BL/BSD plane is the point P, on the basis of four directions (resulting, in this case, in four miniblocks). In this figure, the point P lies within the area B.

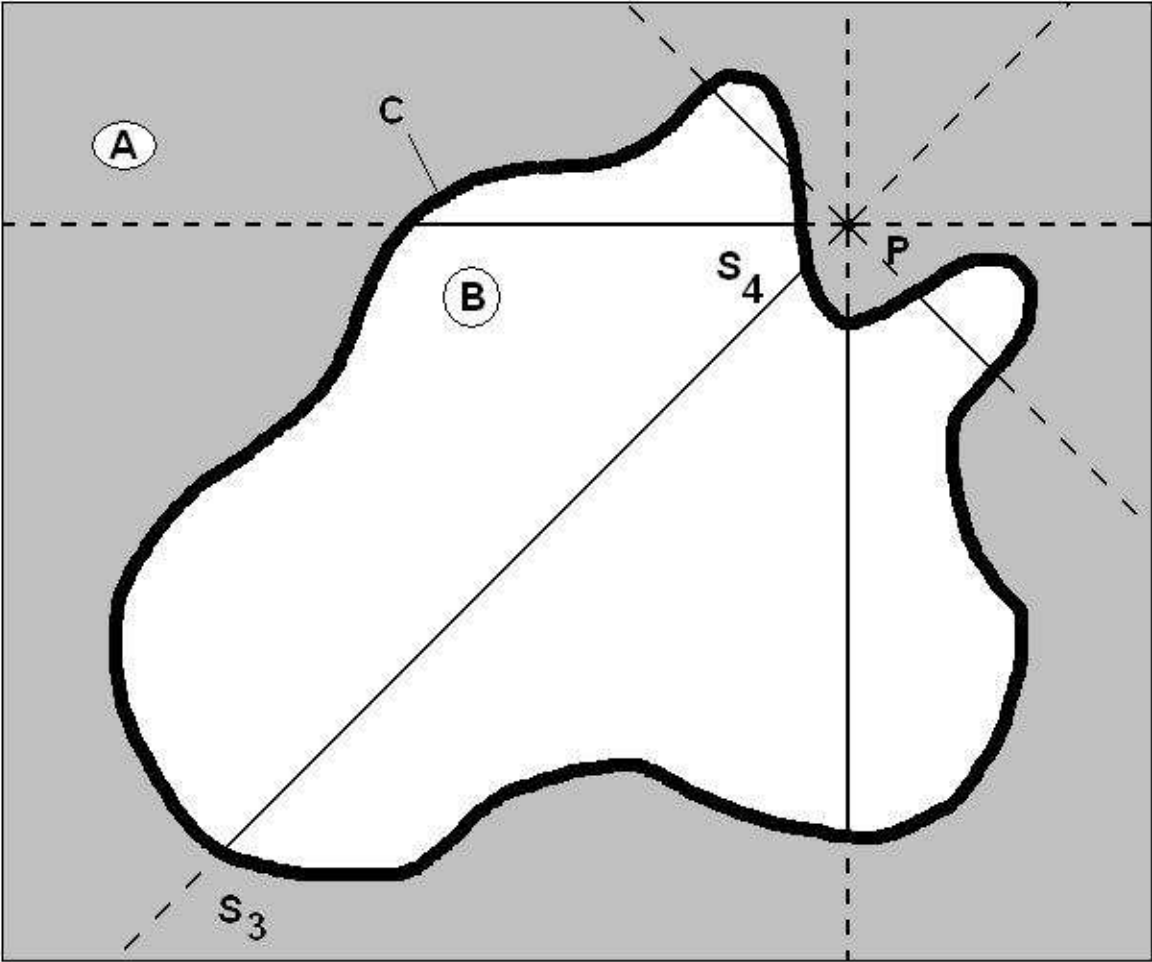


**Figure 5.** Evaluation of the effects of the BL/BSD at the point Q of Fig. 3 (not shown), whose projection onto the BL/BSD plane is the point P, on the basis of four directions (resulting, in this case, in five miniblocks). In this figure, the point P lies outside the area B.

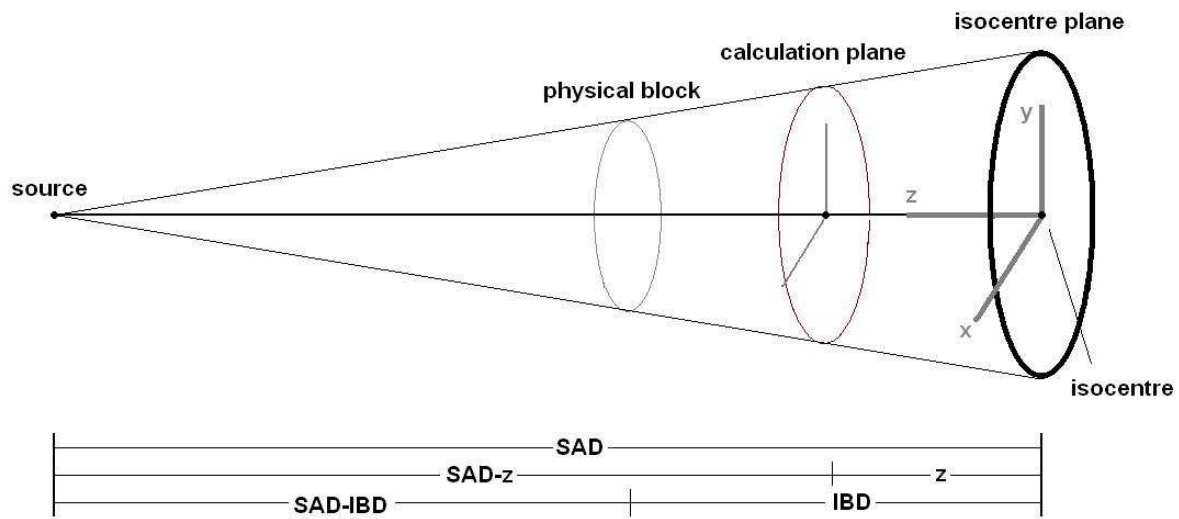


**Figure 6.** The relation between the DICOM block, the extension, and the downstream projection on the  $(x,y)$  plane (calculation plane) at a specified depth  $z$ .

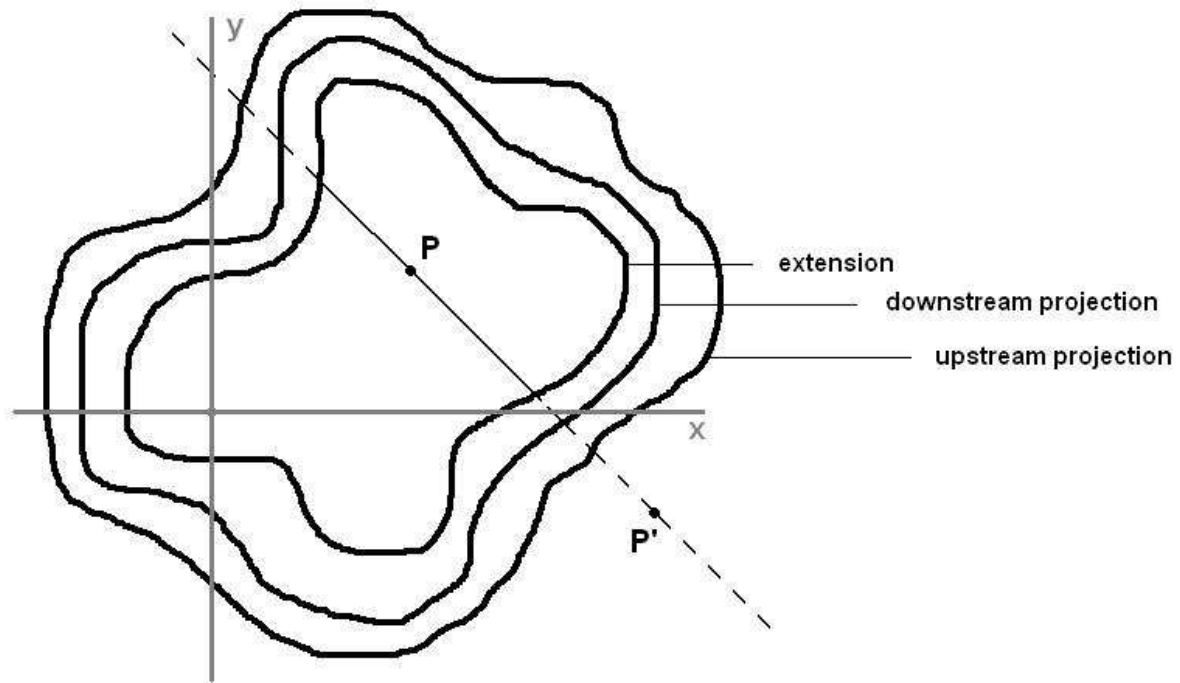


**Figure 7.** The extension and the projections of the downstream and upstream faces of the block on a calculation plane. The point  $P$  lies within the extension, the point  $P'$  without.

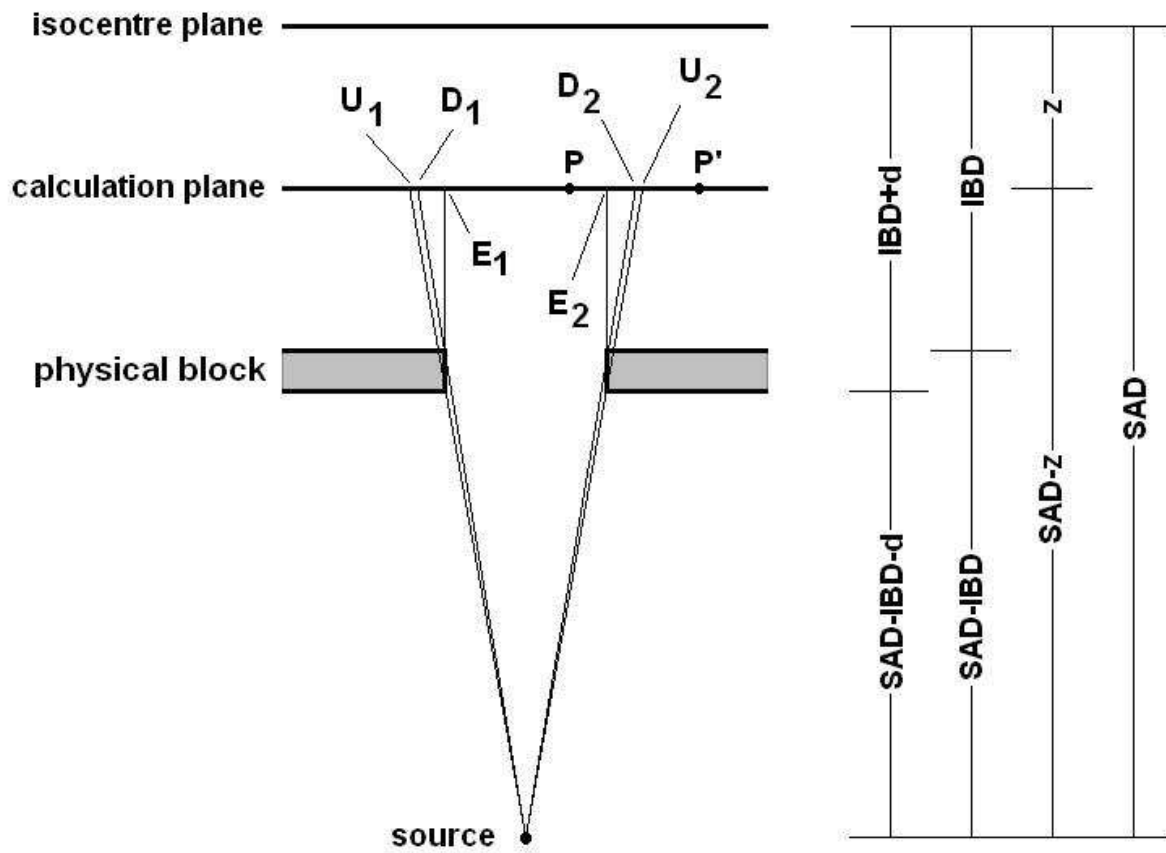


**Figure 8.** The essentials for the evaluation of the contribution of a miniblock to the fluence at specified points (e.g., at  $P$  and  $P'$ ) on the calculation plane.



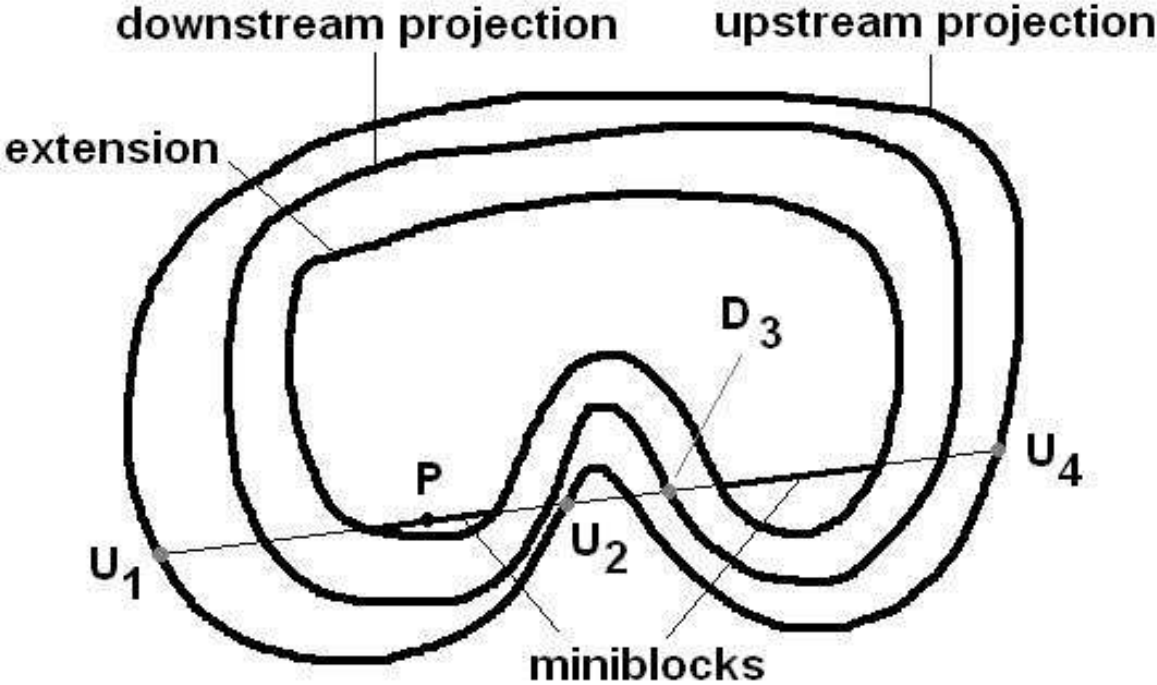


**Figure 9.** Due to one-dimensional nature of the miniblocks, a point lying within the extension (of a miniblock) may also receive contributions which are characteristic to points lying in the exterior of the extension.

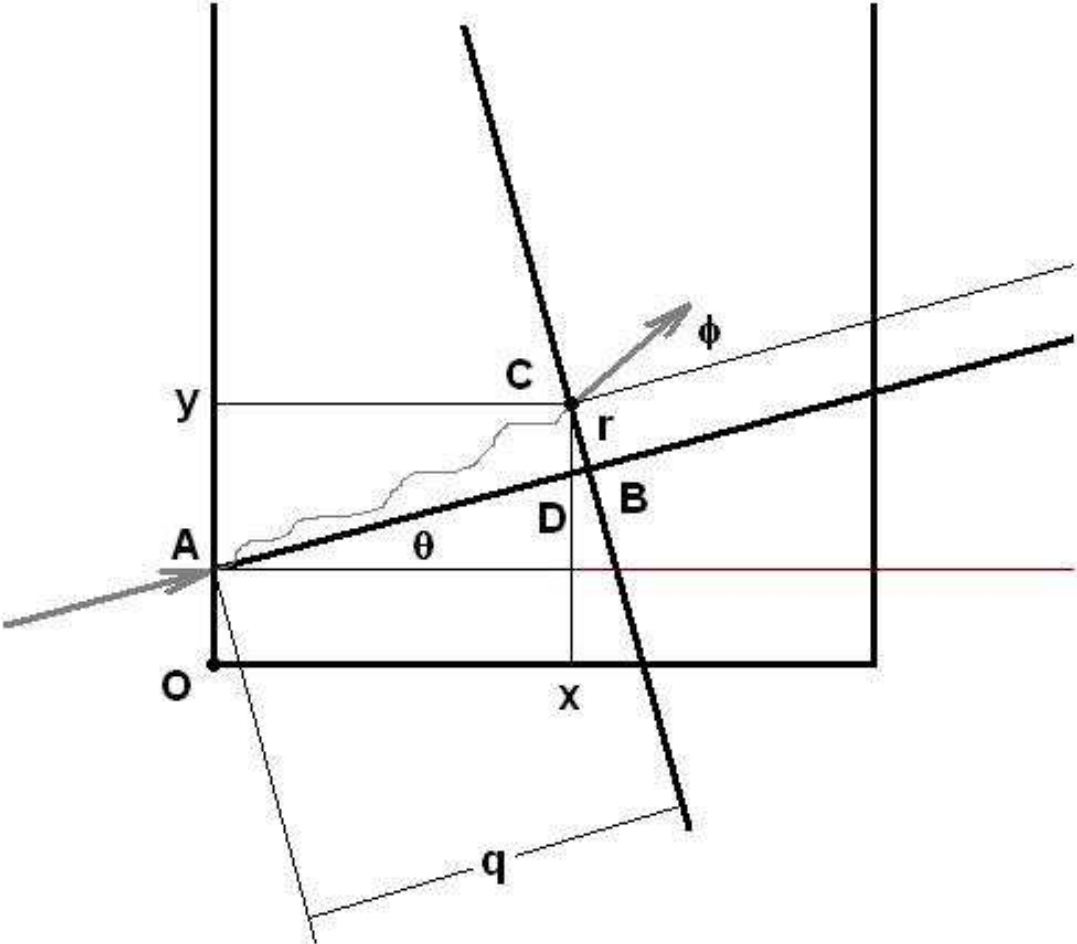


**Figure 10.** The description of the kinematics inside the block. The auxiliary coordinate system introduced in this figure should not be confused with the formal coordinate system of Fig. 6.

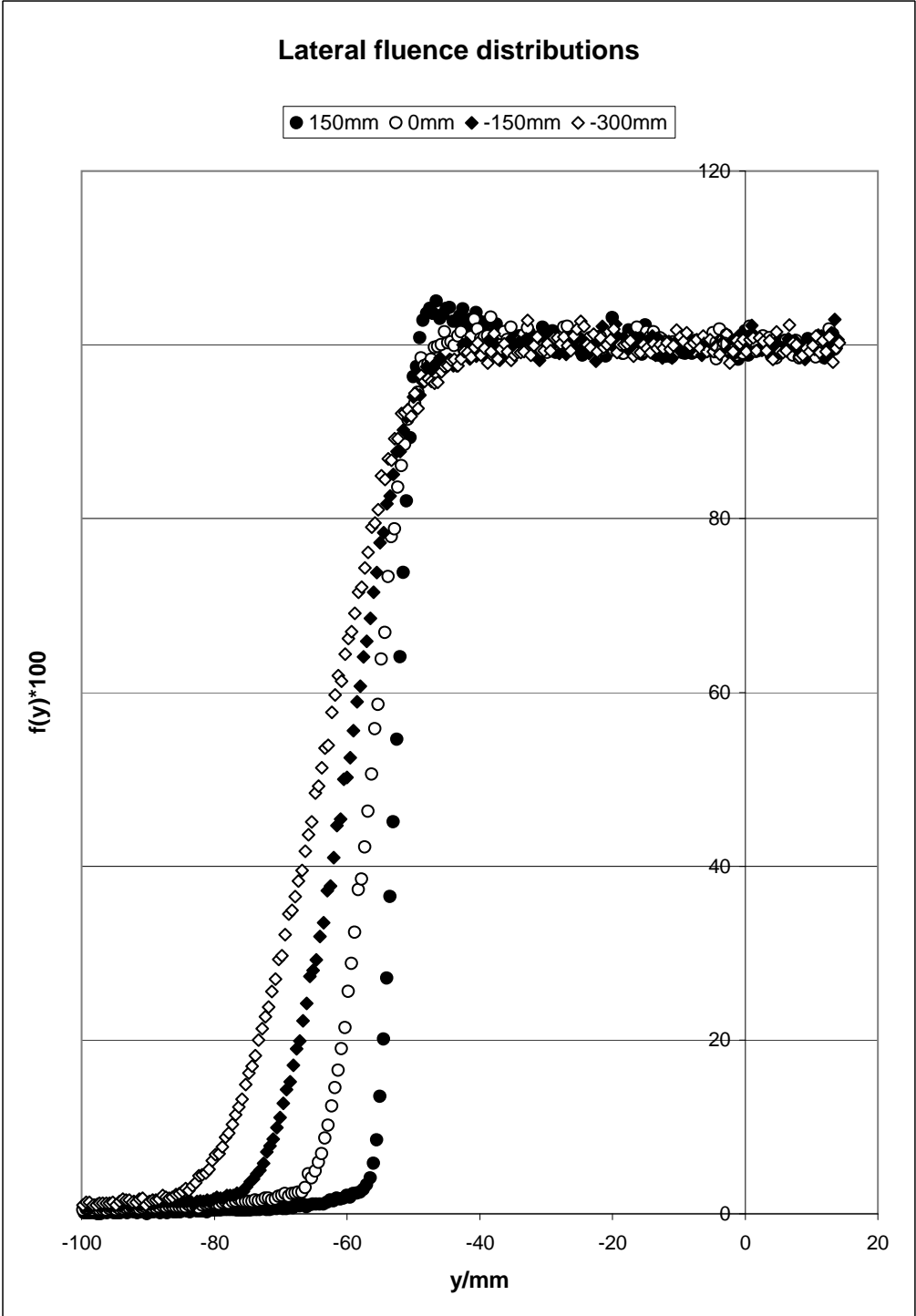


**Figure 11.** The lateral fluence distributions for one energy-NeT combination (171.99 MeV, 154.5 mm) of option 2 of the NCC machine.

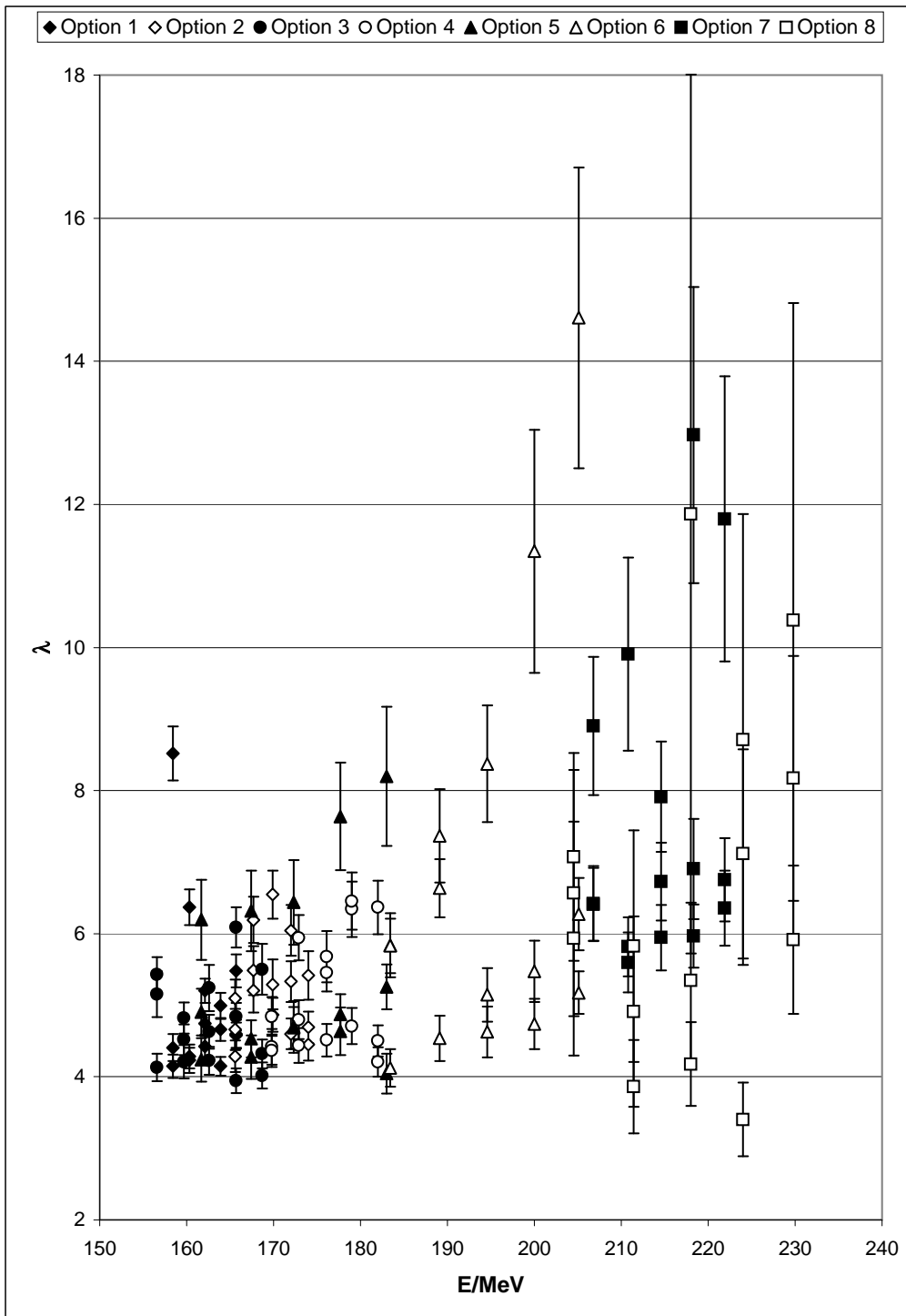


**Figure 12.** The values of the parameter  $\lambda$  for all the energy-NeT combinations of all double-scattering options of the NCC machine.

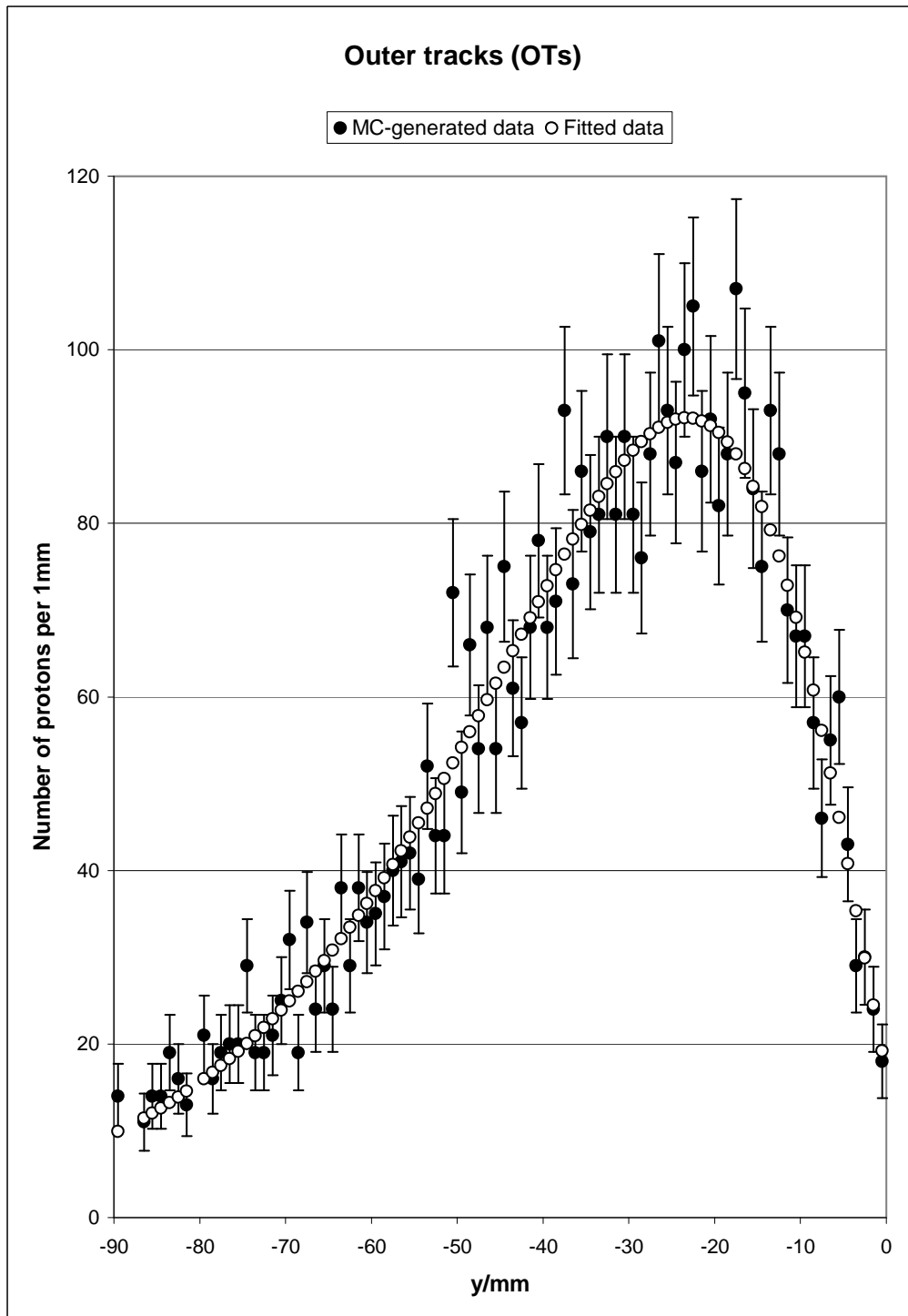


**Figure 13.** A typical description of the lateral fluence distribution for outer tracks. Bins with fewer than 10 entries are not shown.

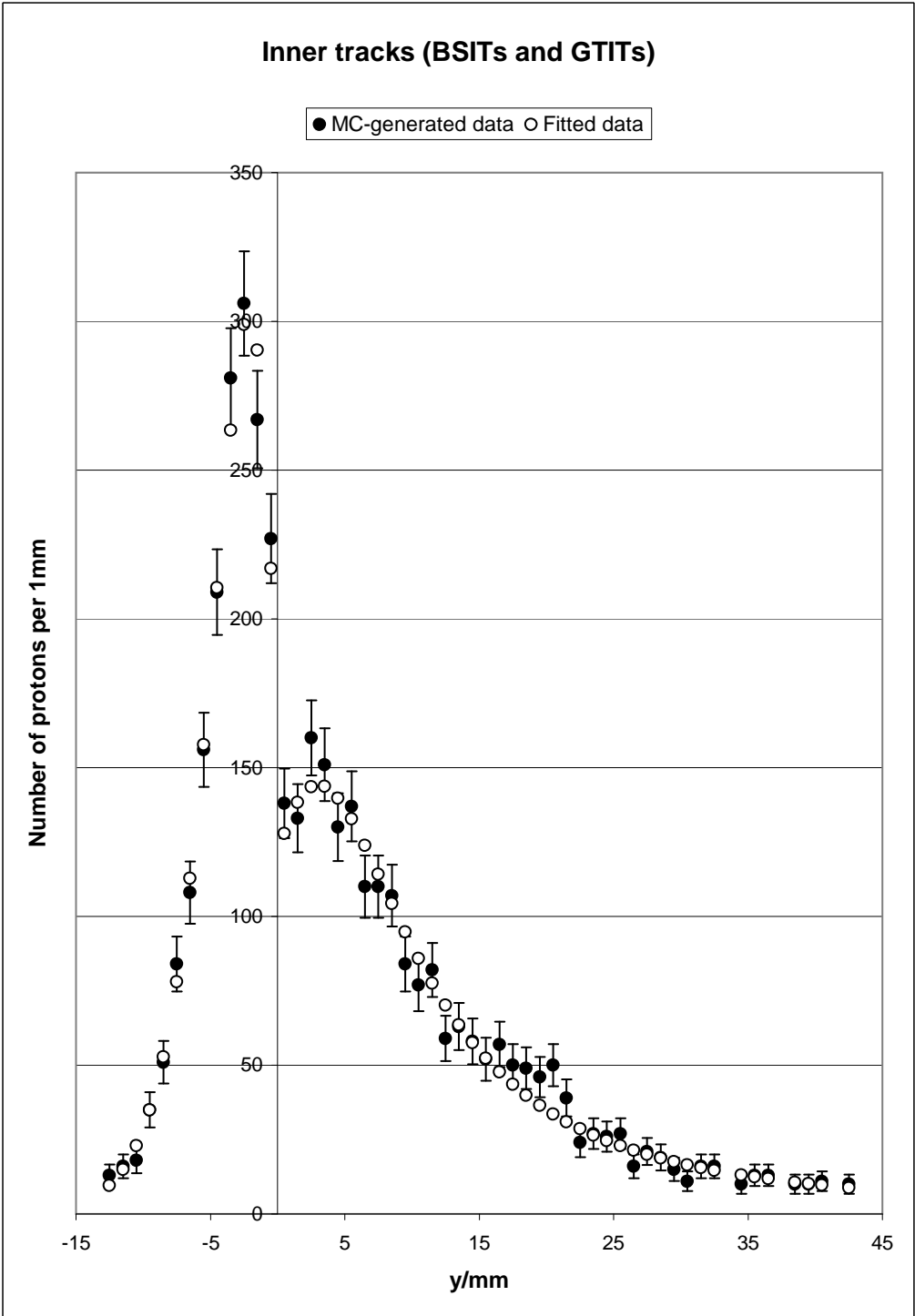
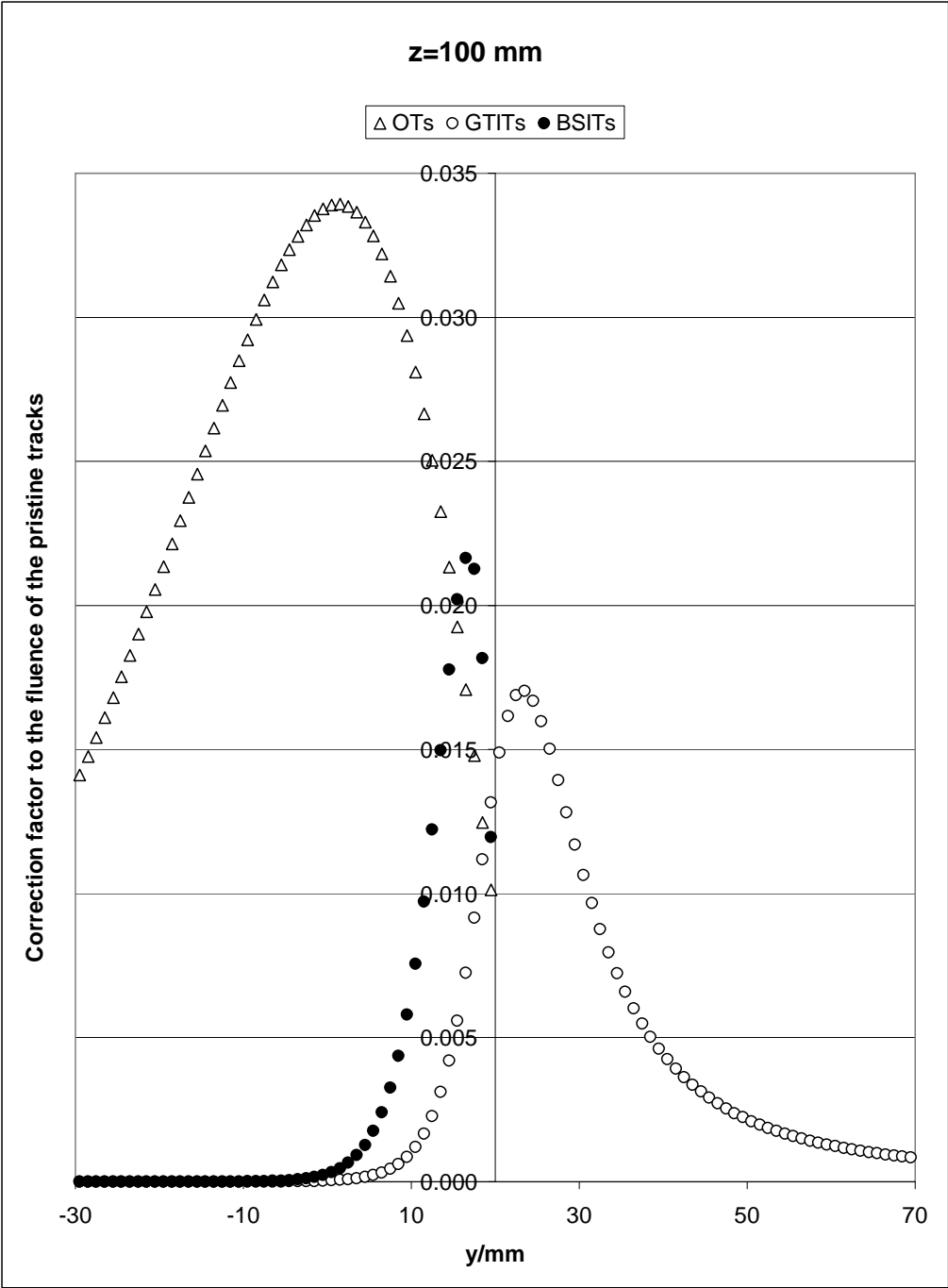
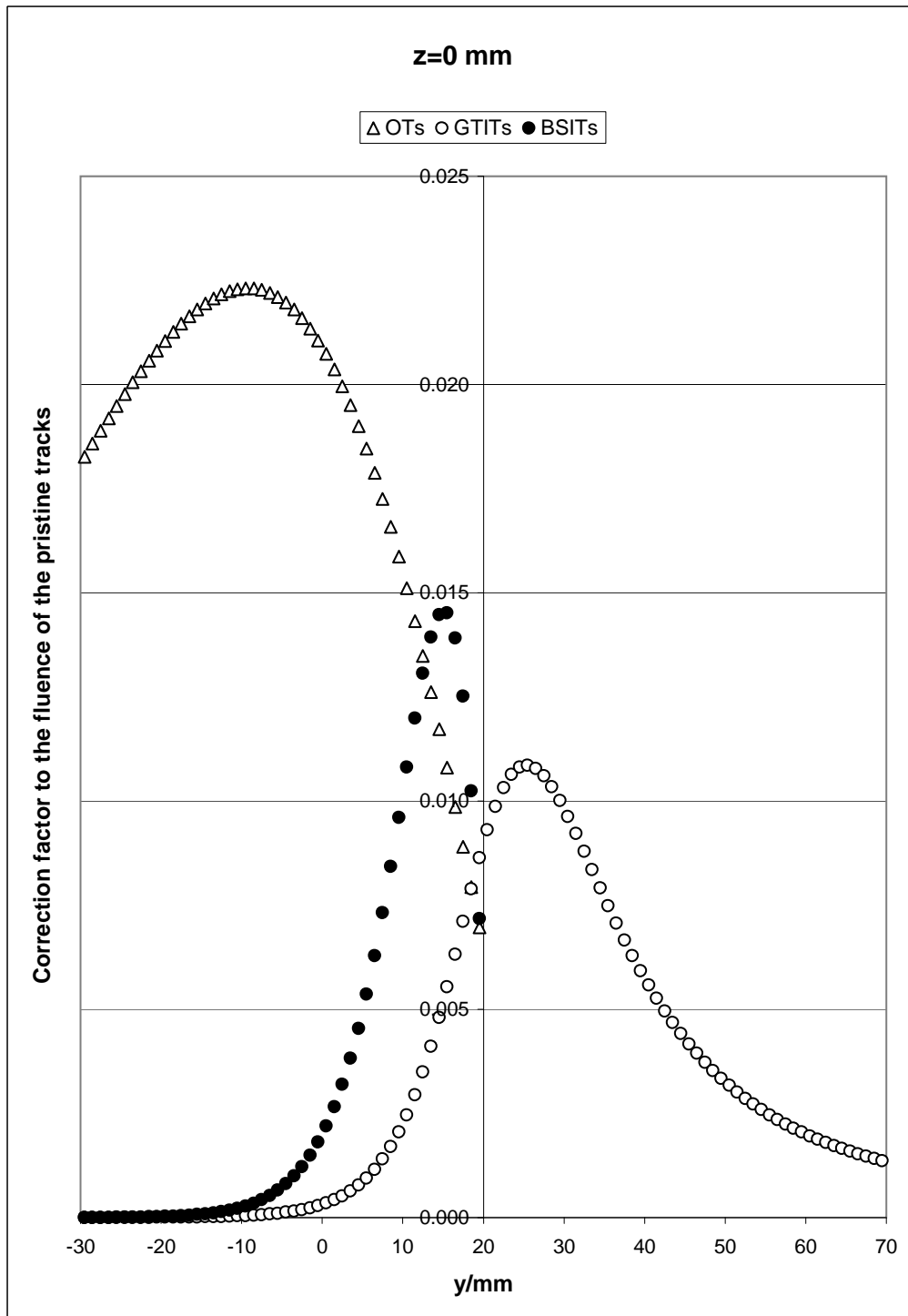


Figure 14. A typical description of the lateral fluence distributions for inner tracks. Bins with fewer than 10 entries are not shown.



**Figure 15.** One case of the scattering corrections (to be applied to the lateral fluence distribution of the pristine tracks) at  $z = 100$  mm. The lateral displacement of the block was  $b = 20$  mm.



**Figure 16.** One case of the scattering corrections (to be applied to the lateral fluence distribution of the pristine tracks) at  $z = 0$  mm (i.e., at isocentre). The lateral displacement of the block was  $b = 20$  mm.



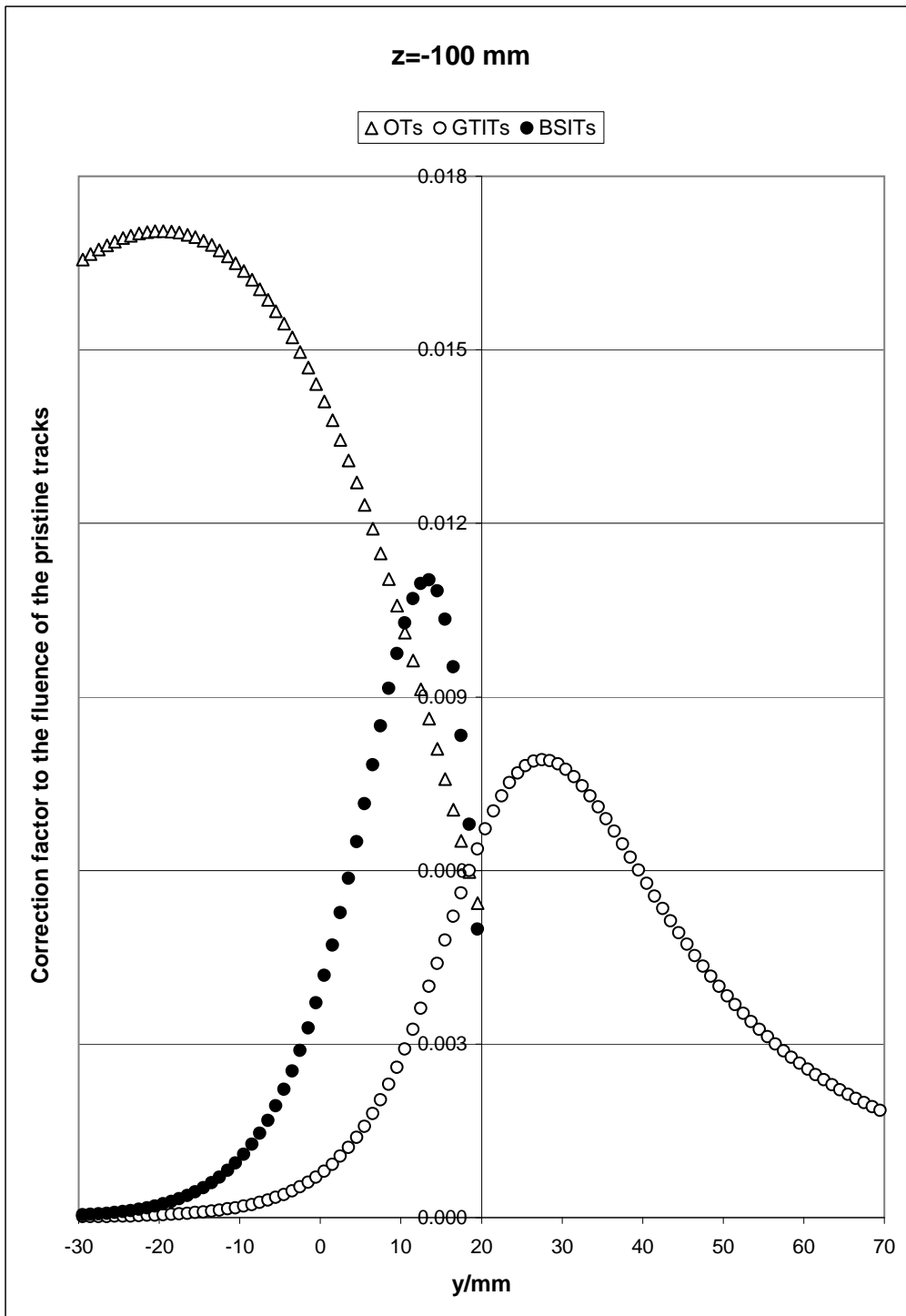


**Figure 17.** One case of the scattering corrections (to be applied to the lateral fluence distribution of the pristine tracks) at  $z = -100$  mm. The lateral displacement of the block was  $b = 20$  mm.

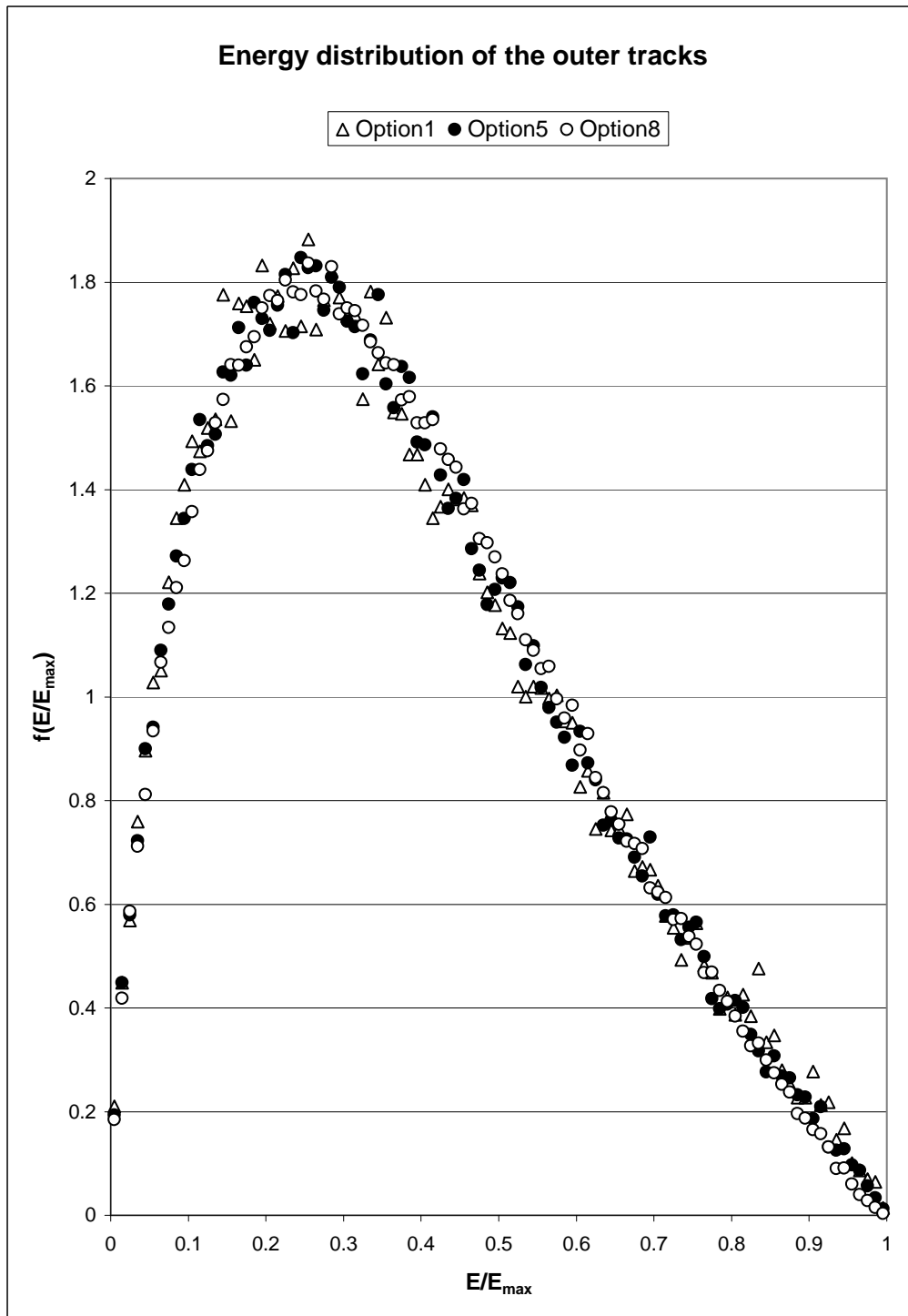


**Figure 18.** The energy distributions for the outer tracks for three energy-NeT combinations of the NCC machine (see text).

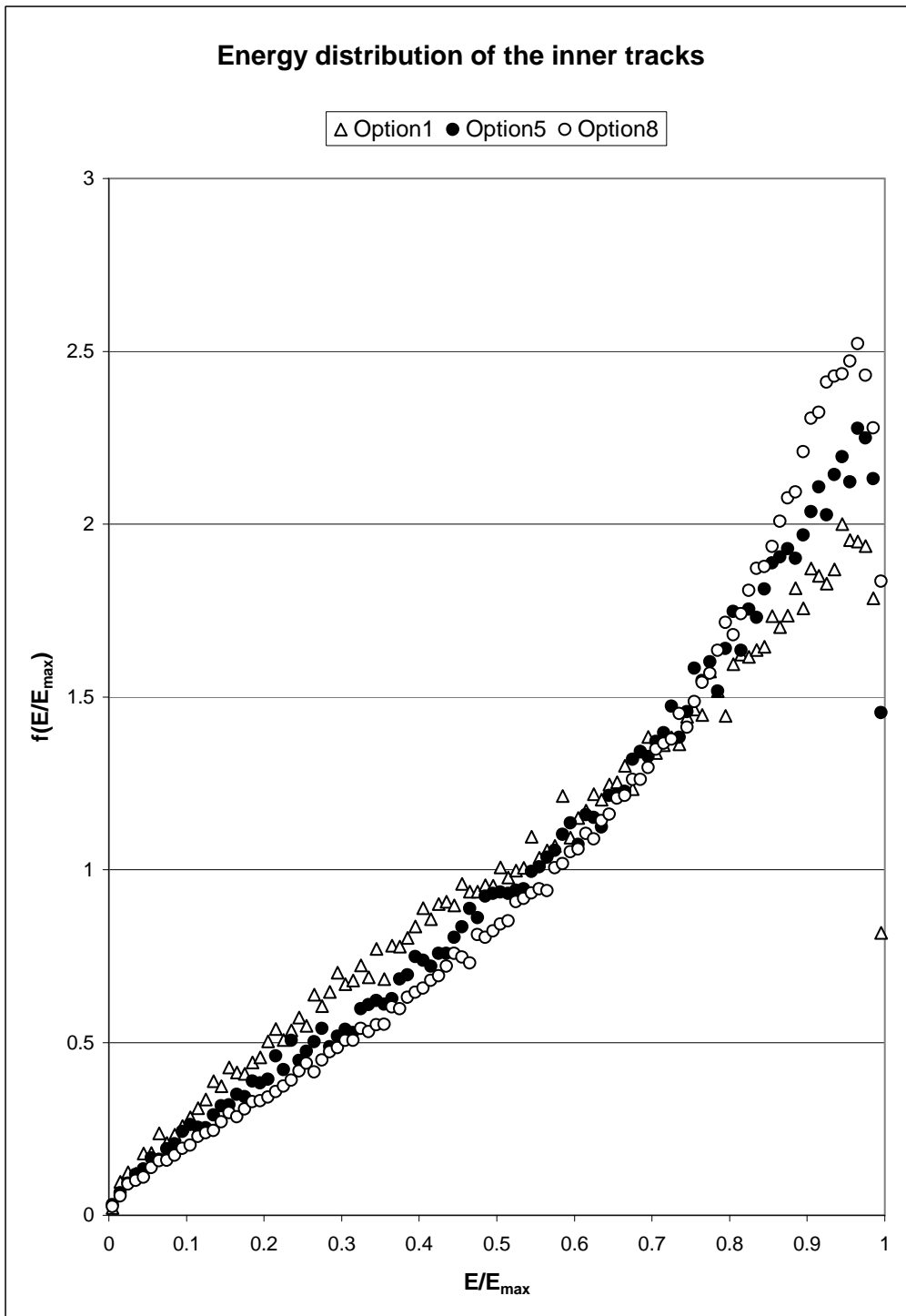


**Figure 19.** The energy distributions for the inner tracks for three energy-NeT combinations of the NCC machine (see text).

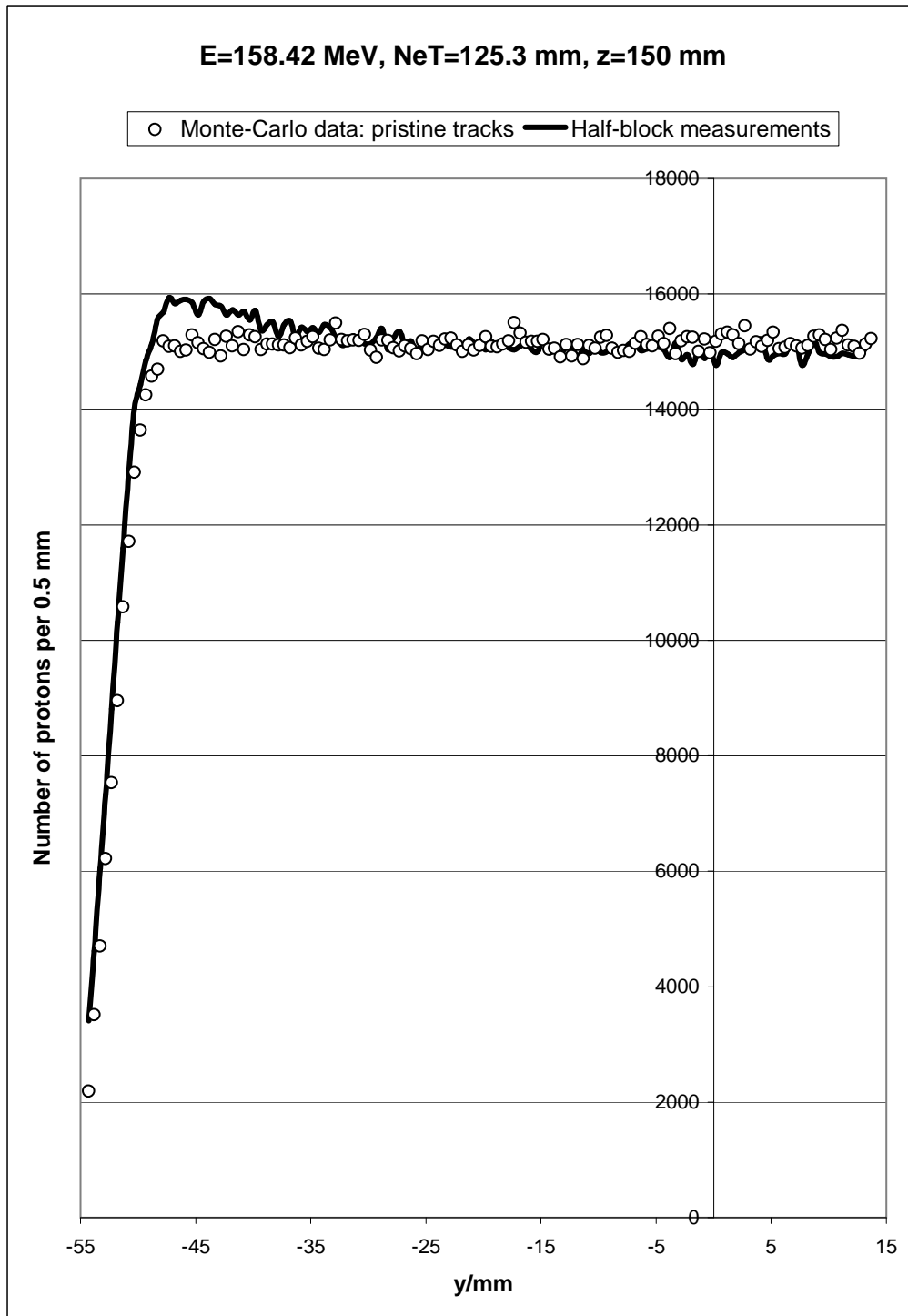


**Figure 20.** The lateral fluence measurements (continuous line) corresponding to one energy-NeT combination of one option of the NCC machine, taken 100 mm away from the downstream face of the block. The Monte-Carlo data shown correspond only to the pristine-beam fluence obtained at the same incident-energy, NeT, and  $z$  values; the measurements have been scaled up by a factor which is equal to the ratio of the

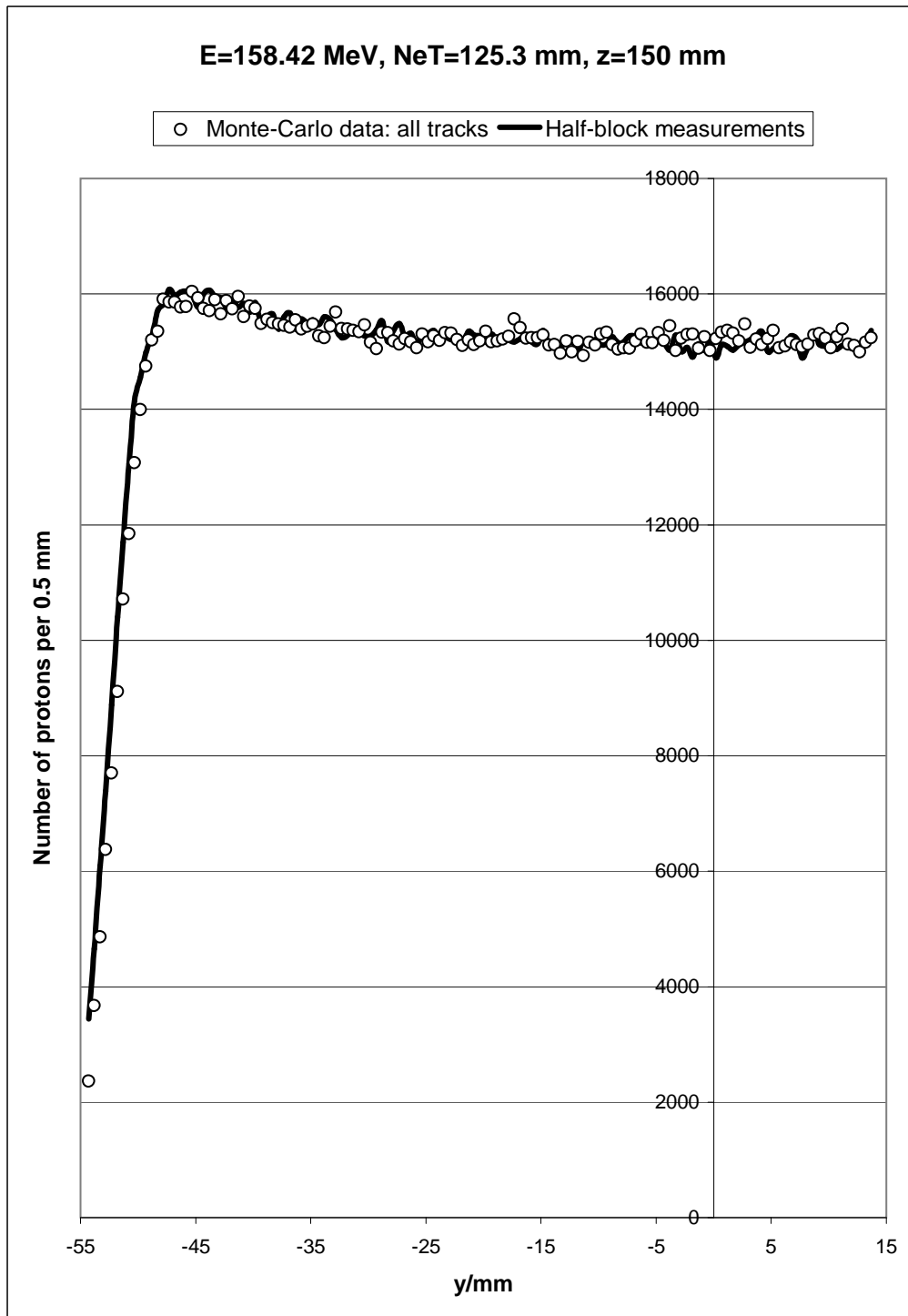


**Figure 21.** The lateral fluence measurements (continuous line) corresponding to one energy-NeT combination of one option of the NCC machine, taken 100 mm away from the downstream face of the block. The Monte-Carlo data shown correspond to the total (pristine-beam plus scattered-protons) fluence obtained at the same incident-energy, NeT, and  $z$  values; the measurements have been scaled up by a factor which is equal

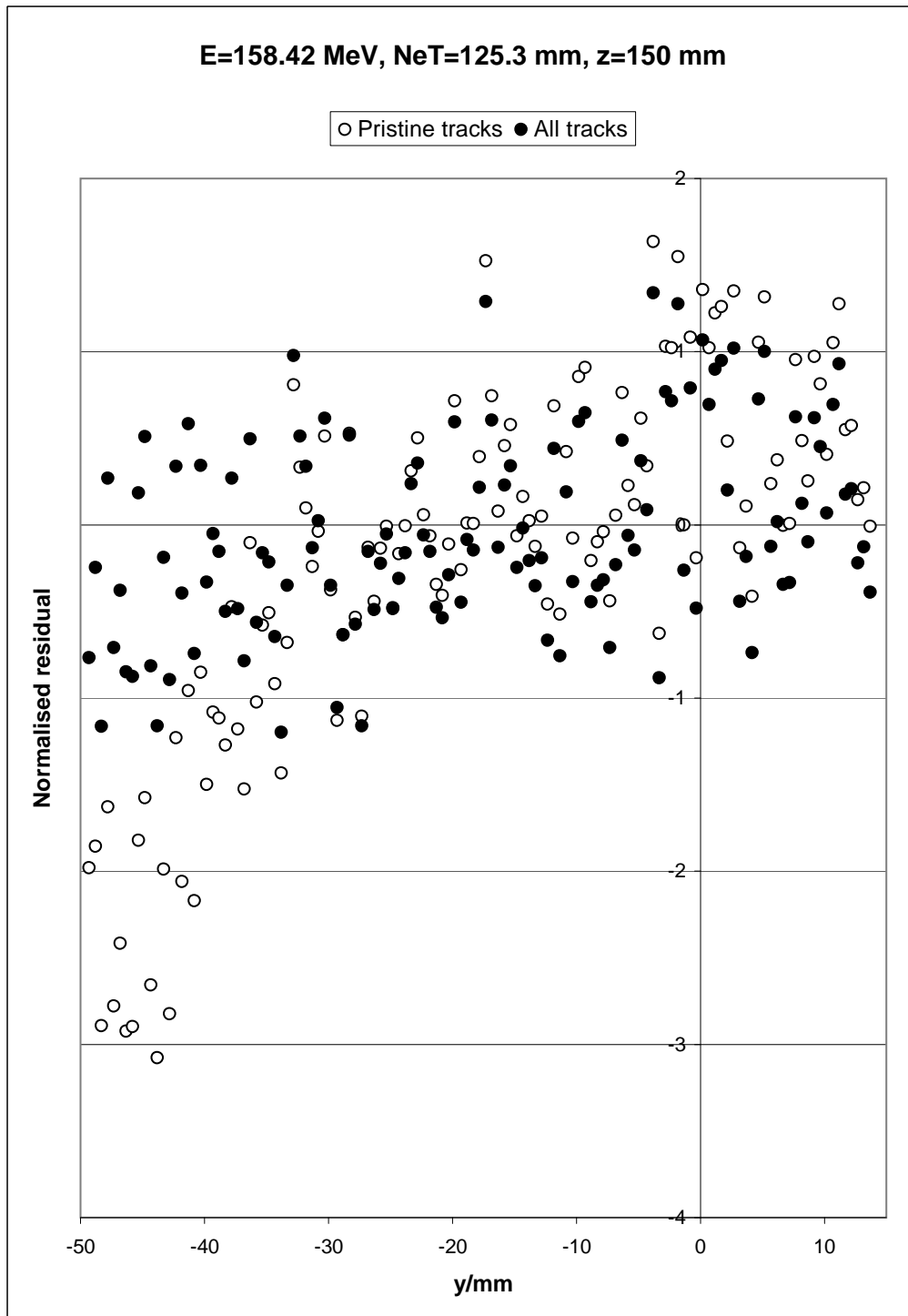


**Figure 22.** An alternative way of displaying the contents of Figs. 20 and 21; shown in this figure are the normalised residuals, plotted versus the lateral distance  $y$ . Evidently, the pristine-beam contribution underestimates the fluence by about 1 to 3 standard deviations for  $-50 \text{ mm} < y < -40 \text{ mm}$ . After the inclusion of the block-scattering effects, the residuals nicely cluster around 0.

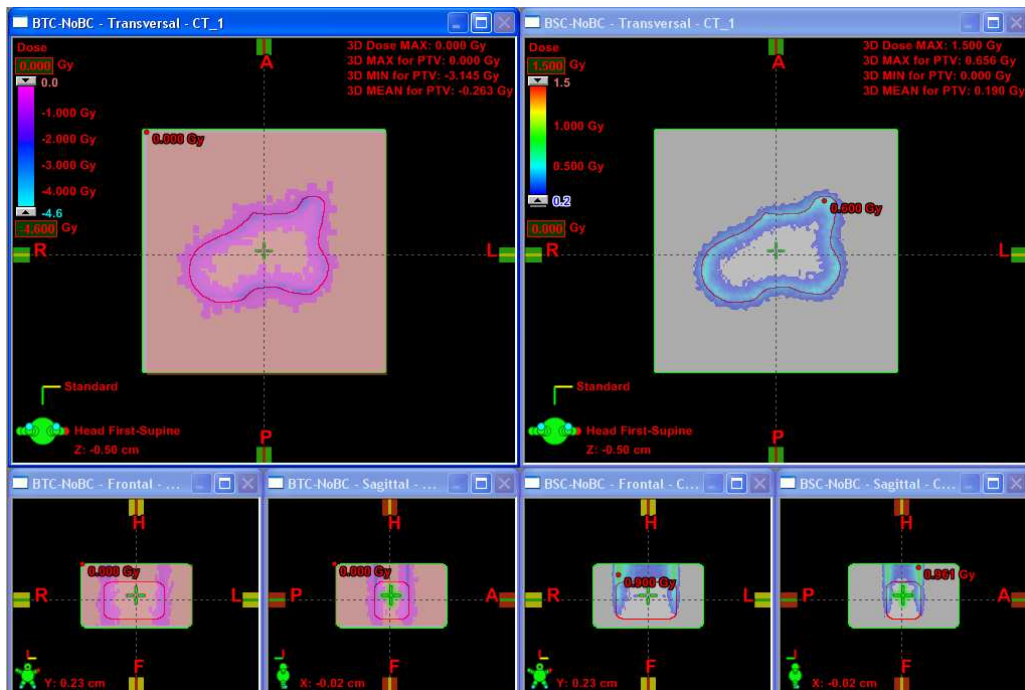


**Figure 23.** The dose contributions corresponding to the block-thickness (on the left) and to the block-scattering (on the right) corrections for the simple water phantom of Section 3.3.



Figure 24. The dose contributions corresponding to both block-relating corrections for the simple water phantom of Section 3.3.